HYDRODYNAMICS OF FLAT PLATES IN CROSS-FLOW NEAR THE FREE SURFACE

Sukruth Satheesh

Hydrodynamics of flat plates in cross-flow near the free surface

Doctoral Thesis

Sukruth Satheesh

Universitat Rovira i Virgili

2019

Hydrodynamics of flat plates in cross-flow near the free surface

Doctoral Thesis

Sukruth Satheesh

supervised by Dr. Francisco J. Huera Huarte

Department of Mechanical Engineering

Universitat Rovira i Virgili
Tarragona 2019

UNIVERSITAT ROVIRA i VIRGILI
Departament d'Enginyeria Mecànica
Escola Tècnica Superior d'Enginyeria Química
Av. dels Països Catalans, 26
43007 Tarragona, Spain
Tel. +34 977 55 96 02 secmec@urv.cat
Fax +34 977 55 96 93 www.etseq.urv.es/DEM/

I STATE that the present study, entitled "Hydrodynamics of flat plates in cross-flow near the free surface", presented by Sukruth Satheesh for the award of the degree of Doctor, has been carried out under my supervision at the Department of Mechanical Engineering of this university.

Tarragona, 2 de abril de 2019

Doctoral Thesis Supervisor

Dr. Francisco J. Huera Huarte

Acknowledgments

I would like to express my gratitude to my advisor, Professor Francisco Huera Huarte for his wise counsel, an unwavering support for conducting research in the field of bluff body fluid dynamics, and for providing me with an opportunity to be a better researcher.

I am also extremely grateful to my parents, who have supported all my aims and ambitions. It is mainly to them that I understood the essence of education– to be a better individual. It is only through their nurturing and encouragement that I have been able to achieve my aspirations.

I would also like to thank Albert, Miguel et al. for inviting me to several fiestas and introducing me to the Spanish lifestyle and culture. The memories of this experience are bound to stay with me for a long time.

Lastly, but not the least, I would like to acknowledge the scholarship grant offered by URV as well as the funding by the Spanish Ministerio de Economía y Competitividad through grant DPI2015-71645-P, without which this research endeavour could not have been undertaken.

Abstract

This thesis presents the results of a study conducted to understand the effect of free surface on forces generated by a flat plate being towed in a quiescent fluid, with the plate surface being normal to the towing direction. The work is based on a parametric study involving aspect ratio, Reynolds number, and submergence depth, with the depth always being measured as the distance between free surface and the upper edge of the plate. Force measurements and quantitative flow visualization techniques have been employed to understand the flow physics. It was found that the drag increases abruptly prior subsiding with increasing submergence depth, with this jump in drag being more prominent in low aspect ratio plates. The abrupt rise in the drag is due to the existence of a gap-flow at the free surface resulting in the formation of a recirculating flow in close proximity to the base region of plate. Overall, the trends are Reynolds number independent, except when the aspect ratios are in the range from 0.75 to 1.33, and the plate was near the free surface.

Furthermore, two different plate configurations have been investigated. First, rigid plates with porosity at distinct locations and secondly structural flexibility. Both concepts have resulted in significant drag reduction, especially near the free surface. The mechanism of drag reduction for porous models has been shown to be due to the interaction between the jets formed at holes, the shear layers and the gap-flow. With structural flexibility, reconfiguration leads to drag reduction.

Publications

Indexed Publications:

S. Satheesh, F. J. Huera-Huarte, *Effect of free surface on a flat plate translating normal to the flow*, Ocean Engineering 171:458-468, 2019 (DOI: 10.1016/j.oceaneng.2018.11.015)

S. Satheesh, F. J. Huera-Huarte, *On the drag reconfiguration of plates near the free surface*, Under Review, 2019

S. Satheesh, F. J. Huera-Huarte, *Effect of porosity at discrete locations on a rigid flat plate translating normal to the flow and free surface*, In preparation, 2019

Conferences:

C. Haëck, S. Satheesh, F. J. Huera-Huarte, (Poster) *Drag forces on a flat plate towed near the free surface*, Workshop on Fluid Mechanics, Tarragona, Spain, 2017

S. Satheesh, C. Haëck, F. J. Huera-Huarte, *Effect of the Free Surface on the Drag Forces on a Flat Plate Translating Normal to the Flow*, ASME 2018 37^{th} International Conference on Ocean, Offshore and Arctic Engineering, Madrid, Spain, 2018 (OMAE2018-77646)

S. Satheesh, F. J. Huera-Huarte, *Effect of free surface on a flat plate translating normal to the flow*, Workshop on Fluid Mechanics, Málaga, Spain, 2018

S. Satheesh, F. J. Huera-Huarte, *The effect of the free surface on the thrust production of a flexible pitching foil*, 12^{th} European Fluid Mechanics Conference, EFMC12, Vienna, Austria, 2018

S. Satheesh, F. J. Huera-Huarte, (Poster) *Effect of free surface on the drag forces generated by flexible foils translating normal to the flow*, First Colloquium of the Spanish Theoretical and Applied Mechanics Society (STAMS2019), Madrid, Spain, 2019

Contents

List of Figures

List of Tables

Nomenclature

AR	Aspect Ratio, ratio of square of the span to the exposed area
B	Blockage ratio, ratio of model exposed area to that of the test-section
C_D	Coefficient of drag
C_Y	Cauchy number, ratio of inertia force of fluid to elastic force of material
D_h	Hydraulic diameter, ratio of plate wetted area to perimeter
DNS	Direct Numerical Simulation
DPIV	Digital Particle Image Velocimetry
E	Modulus of Elasticity
Fr	Froude number, ratio of inertial force to gravity force
I	Sectional moment of inertia
$\Re$	Reconfiguration number, ratio of foil force to plate force- infinite domain
$\Re^*$	Reconfiguration number depth based, ratio of foil force to plate force
RANS	Reynolds Averaged Navier-Stokes
Re	Reynolds number, ratio of inertial force to viscous force
RPM	Revolutions Per Minute
U	Velocity

b	span
c	chord
d	submergence depth
e	thickness
l	cantilever length
n	loading exponent
q	Load per unit length
t^*	non-dimensional time
u	foil deflection

Greek operators

β	Porosity, ratio of open area to total area
∞	freesteam
ρ	Fluid density
ν	Kinematic viscosity of the fluid
ω	Vorticity
Υ	Vogel exponent

Chapter 1

Introduction

Boats and ships have always played an important role in human activities. Although their designs have evolved over centuries, they are nowhere near to the natural systems, both in terms of performance as well as design. Nature has had thousands of years to optimize the design and functional traits of organisms through evolution but our lack of understanding of the physics involved in these systems is a major limitation. The effect of free surface on the forces generated being one such phenomenon. It is expected that only through a better understanding of the fluid-structure interaction involving the free surface can help us achieve not only huge improvements in current marine structural and naval designs through drag reduction but also develop newer modes of underwater propulsors for Autonomous Underwater Vehicles (AUV), and devices for harvesting of energy from renewable sources, like tides and surface waves.

1.1 Background

The study of forces generated by bluff bodies has been one of the oldest problems in fluid mechanics. Cylinders and flat plates oriented

normal to the flow exemplify bluff bodies owing to large regions of separated flow and a significant pressure drag component. The free streamline theory (hodograph plane) applied to two-dimensional flat plates held normal to the flow by von Helmholtz (1868) and Kirchhoff (1869) have been the earliest works to characterize the flow properties such as velocities and wake pressures and the consequent forces acting on the body. This was followed up by Roshko (1954) with a modified version of the hodograph plane theory to accommodate arbitrary base pressures and obtain better results. There is a good amount of literature on the interaction between cylinders and boundaries, but very little information is available related to the interaction between flat plates and deformable boundaries. Miyata et al. (1990) conducted experimental and numerical studies on the flow around a horizontal circular cylinder with its axis normal to the flow, located beneath the free surface. They found a decrease in drag with increasing proximity to the free surface, and attributed to an asymmetric vortex shedding process and their mutual interaction. Other researchers have also studied the interaction of circular cylinders and a free surface such as Sheridan et al. (1997), Reichl, P., Hourigan, K., Thompson (2005) and Bouscasse et al. (2017). Cylinders however present no edge discontinuities and have flow separation points that are Reynolds number dependent, unlike thin flat plates held normal to the flow with fixed separation points at the edges. Dennis and Chadna (1995) investigated numerically the steady 2D flow across a normal flat plate in an infinite domain at very low Reynolds numbers

(Re). They found that the vortex cores traverse increasingly downstream with Reynolds number, with the vortices remaining attached to the plate. Koumoutsakos and Shiels (1996) studied 2D viscous, incompressible flow across a normal flat plate undergoing impulsive or uniformly accelerated motion (Re_b=20–1000) using an adaptive vortex method to compute the drag coefficient. They found that an impulsively started plate generates a stable vortex configuration due to the shear layer roll-up, while the uniformly accelerated plate generates a Kelvin-Helmholtz type instability due to the increased strength of the shear layer, resulting in the formation of multiple vortex centres, dependent on the acceleration magnitude. Several other researchers (Hudson and Dennis (1985), Dennis et al. (1993), Najjar and Vanka (1995b), Hemmati et al. (2016b)) have studied numerically, using different techniques the shedding process and the wake characteristics of two-dimensional flat plates and the low-frequency fluctuations in the lift and drag. Plates of finite span involve complex three-dimensional flow phenomena which cannot be captured accurately with 2D simulations, as indicated by Najjar and Vanka (1995a) and Najjar and Balachandar (1998) through their 3D DNS studies on a flat plate of aspect ratio (AR) of 6 placed normal to the flow at a $Re_{D_h} \approx 1700$ and 400, with periodic boundary conditions along the span. They found that the vortex break-up and shear layer extension occur further downstream in 3D simulations and attributed it to secondary flow instabilities. Narasimhamurthy and Andersson (2009) also conducted 3D DNS studies on a similar configuration at

a Re_{D_h} of 1300, but with a finer mesh compared to the former. They found that a base pressure reduction caused an increase in the shedding frequency and produced a shorter recirculation bubble. These results indicated the importance of conducting 3D numerical studies even when the geometry is 2D, and provided a greater understanding regarding the flow and its instabilities, but they still fail to account for the vortex shedding from the other 2 edges of the plate and their effect on the force. Hemmati et al. (2016a) found through their DNS studies at a Re_{D_h} of 1830 on a thin flat plate ($AR = 3.2$) and its comparison with a 2D plate that the additional 2 shear layers in the 3D plate resulted in an increased shedding frequency, smaller recirculation zone, reduced drag, an absence in the drift in lift and drag values, and suppression of the spanwise secondary instability. This was attributed to the difference in the shedding process denoted as peeling, wherein vortices are shed alternately by the adjacent mutually perpendicular sides.

Fage and Johansen (1927) conducted one of the earliest set of experiments on a flat plate connected floor-to-floor ($AR \approx 14$) and at various inclinations, at a $Re_{D_h} = 1.5{\cdot}10^5$, and estimated drag coefficients when the flow is normal to the plate. The deviation from theoretical solution was attributed to the greater shear layer velocity over the freestream. Winter (1936) also presented a trove of data in his technical report linked to the forces generated by airfoils and flat plates of various aspect ratios and planforms. Fail et al. (1959) studied the effect of aspect ratio and geometries on the drag gener-

ated when the flow was normal to the plate, that had aspect ratios in the range 1 to 20, in experiments conducted at Re_{D_h} in the range from $1.6{\cdot}10^5$ to $3.7{\cdot}10^5$. They found the effect of geometry to be insignificant compared to the aspect ratio and the existence of two shedding frequencies for a rectangular plate; one associated with the smaller plate dimension and a lower frequency associated with the longer dimension. Lisoski (1993) studied the effect of aspect ratio for nominally two-dimensional flows across a normal flat plate at low Reynolds numbers and found that a minima exists in the drag generated at high AR, which was attributed to a symmetric wake bubble. But with one end free, no such minima was observed, indicating the significant influence of the tip. Ringuette et al. (2007) investigated semi-infinite flat plates at two different aspect ratios and their results not only verified Lisoski's observations but also presented information regarding the evolution and interaction of the lower tip vortex with the side vortices. Malavasi and Guadagnini (2007) studied the effects of free surface on the force generated by a rectangular cylinder with its axis along the flow direction, at various Reynolds numbers experimentally. They found that boundaries, rigid or flexible have a higher effect on lift than drag. The lift force changed in direction and magnitude significantly as the distance between the cylinder and free surface reduced, and its dependence on Reynolds number attributed to the free surface distortion.

However, not much information is available regarding the mechanism of force modulation in the presence of boundaries. Ortiz et al. (2015)

conducted wind tunnel tests to study the dynamics of flat plates with AR ranging from approximately 0.1 to 2.5, over a range of incidence angles at a fixed wind speed, with the plate being located either in close proximity to the wall or far from it. It was found that the drag coefficient calculations were in reasonable agreement with the modified theoretical equation of Gould (1969), (ESDU, 1970) when the plate was normal to the flow. Fernando and Rival (2016b) studied the force and vortex ring dynamics of thin elliptical and rectangular plates with aspect ratios ranging from 1 to 4, of a constant hydraulic diameter. They found that the drag force of the $AR = 1$ circular plate was the lowest due to the interaction of the vortex ring with the plate. The $AR = 1$ square plate also presented lower drag when compared to other rectangular plates but higher than the circular one. This was attributed to the faster spanwise and downstream convection of the ring, and resulted in reduced interaction. Another observation indicated by them was that at higher aspect ratios, corresponding elliptical and rectangular plates showed minimal difference in trends of force and the shed vortex rings. This demonstrated that the edge discontinuities are not very significant compared to AR. In another paper by Fernando and Rival (2016a), the authors studied experimentally elliptical plates with AR ranging from 1 to 2, with a constant hydraulic diameter in order to determine the reason for extensive appearance of propulsors with AR greater than 1 in biological entities. It was found that plates with AR greater than 1.5 were insensitive to Reynolds number and presented peaks in the force

signals, indicating a better suitability for manoeuvring and braking situations, whereas the $AR = 1$ plate produced lower force due to enhanced vortex ring-body interaction. Liu et al. (2016) performed 2D simulations of flow past a normal plate near the free surface at 5 different submergence depths and found that the drag decreased with depth i.e., drag was lowest at the free surface and highest when away from it, and attributed to the change in the vortex shedding pattern and frequency. A jet-like flow originating from the free surface was seen to merge with the vortex shed from the lower tip and dissipate in the wake whereas no such phenomena was observed when the plate operated far from the free surface, similar to Miyata et al. (1990). Sumner et al. (2003) and Hémon (2017) studied the dynamics of various kayak paddles under several configurations and compared their performance against a flat plate. They found that all paddle profiles had distinct attributes which made them suitable at particular operating regimes, but altogether, most of the paddles had lower drag than a flat plate when placed normal to the flow.

With drag reduction being highly relevant for better energy efficiency, several techniques have been tested for streamlined bodies, ranging from vortex generators and chemical coatings to even active flow control. However, this kind of study is lacking in bluff bodies, especially with regards to normal plates. Castro (1971) conducted one of the earliest studies involving plates with perforations and their effect on drag, and found that porosity (β) plays a significant role in drag generation with an inverse relationship between drag coefficient

and porosity due to the motion of the recirculation region further downstream. Roberts (1980) conducted studies on series of slotted circular disks at high Reynolds numbers and found that the location of the holes apart from porosity plays a strong role in drag generation. Perera (1981) studied the wakes of solid and porous fences in an atmospheric boundary layer and found that the location of the recirculation bubble moves further downstream in case of porous fences when compared with that of a solid fence. Several subsequent works have studied the effect of porosity, but with a viewpoint of characterizing the turbulent flow-fields generated downstream, for example Chen and Jirka (1995); Kim and Lee (2001). Malavasi et al. (2012) conducted experiments on pressure losses in circular pipes with different perforated plates and found that the hole location and number of holes have a strong effect on the pressure drop. Huera-Huarte (2014) conducted experiments on paddle racquets with several porosity values and their distribution across the racquet head to understand and quantify the effect of holes on the aerodynamic performance and found that a distribution of the holes closer to the racquet periphery yielded lower drag values. Theunissen and Worboys (2018) have recently performed experiments involving drag and wake measurements of circular disks over a range of porosities and their spatial distribution. They found no coherent link between the spatial distribution of the holes and the drag coefficient, but the aspect of porosity plays a dominant role. They also found that the hole jets generally deviated from their axes to merge with the outer shear layer, with this inter-

action being highly three dimensional and stronger with increasing proximity of the holes to disk edge. Wave absorbers or breakwaters are structures developed for minimizing wave reflection and utilized frequently in wave tanks as well as harbour walls as a coastal barrier, with their designs involving a series of vertical or inclined plates with holes, with several factors such as number of plates, their spacing and individual porosities playing a significant role in determining absorption efficiency (see Tuck (1975); Yu and Chwang (1994); Cho and Kim (2008) for more details). Since the literature involving the effect of porosity and its spatial distribution are only available for circular disks and wave absorbers, its efficacy for rectangular plates and in the environment of free surface has not been established.

Another parameter of importance is the flexibility of the body. Structural flexibility is ubiquitous in nature, be it flora or fauna. It has always been used as an asset for enhancing the exposed area of the leaves thereby increasing the area for photosynthesis as shown by Niklas (1992) in his simulations, or for reducing the drag generated due to steady or unsteady fluid loading, which in turn has been studied over the years since the fundamental work of Vogel (1984). The work by Vogel suggested that an increase in fluid velocity results in a change in the quadratic relationship between drag force and velocity ($F \propto U^2$) to a benign relationship of $U^{2+\Upsilon}$, where Υ is the Vogel exponent and is negative, due to the reduction in the exposed area and streamlining. Vogel (1989) showed that the increase in velocity results in rolling up of the leaves of the trees into cones and reduced

the cross-sectional area, generating lower drag. This process of drag reduction through the manipulation of the exposed area is known as reconfiguration. Harder et al. (2004) studied a few aquatic plant species and confirmed the importance of reconfiguration as an adaptation for survival. Alben et al. (2002, 2004) presented theoretical and experimental results on reconfiguration of fibres in soap films and attainment of self similar bending profiles which contribute to drag reduction. They found that Υ shifts from 0 to -2/3 as the fluid loading is increased with respect to fibre rigidity. Ghisalberti and Nepf (2002) studied the effect of a mixing flow on aquatic plant canopies and its effect on plant motion. They found that the Kelvin-Helmholtz instabilities generated by the flow profile caused a coherent waving of the plant structures, with high vertical transport of momentum. Gosselin et al. (2010) conducted significant amount of experiments to study the drag reduction of flexible plates and developed models to explain the reconfiguration process. They found that the results of reconfiguration for finite width plates to be similar to that presented by Alben et al. (2004) for fibres in soap-film, indicating it to be mostly two-dimensional, and the asymptotic Vogel exponent to be -2/3 by dimensional analysis. In fact, the drag-velocity scaling behaviour was studied using a non-dimensional parameter for the rigidity, the Cauchy number (C_Y), which is the ratio of inertial force acting on the model to the elastic force offered by the material and scaled with the drag coefficient of a rigid plate (C_{D_0}) of the same dimensions. They found that the force generated decreases with increasing Cauchy num-

ber. Luhar and Nepf (2011) conducted theoretical and experimental studies of flow induced reconfiguration on buoyant structures that mimic seagrass, both in terms of stiffness and buoyancy. Their studies for structures without buoyancy reinforced the previous results of drag-velocity scaling transitioning from quadratic to almost linear, but with buoyancy as a significant parameter, the scaling might even be sub-linear up to a certain extent. Leclercq and de Langre (2016) presented results from numerical simulations involving different flow profiles across cantilevers of varying cross-section and proved that the scaling of drag with velocity can be obtained using power law approximations.

1.2 Present work

Based on the limited amount of literature available pertaining to the effect of free surface and bluff bodies in general, this work focuses on understanding its effect on normal rigid plates. The shape/orientation of the plates, and the effect of Reynolds number has been looked at in order to understand its behaviour over a range of submergence depths measured from the free surface. This has been followed up with experiments involving flexible structures in order to characterize the effect of bending rigidity on the horizontal forces and finally, experiments involving strategically located holes on rigid plates and their effect on drag, all within the realm of understanding the effect

of free surface on plates translating normal to the flow. Additionally, qualitative as well as quantitative flow visualization techniques have been used to analyse the wake structure and correlate the forces with flow.

1.3 Thesis layout

The thesis is organized with Chapter 1 laying the groundwork by providing an introduction to the topic, presenting the state of the art, the voids in knowledge, and the current research objectives. Chapter 2 enumerates the experimental facilities used, and the instrumentation employed for characterizing the phenomenon. Chapter 3 discusses the results obtained for the rigid plates, Chapter 4 for flexible foils, and Chapter 5 for a rigid plate incorporating porosity at strategic junctures, with each of these chapters being independent works of study which have either been published or the manuscripts are being prepared for publishing in scientific journals. Finally, Chapter 6 summarizes the overall work and suggests recommendations for future course of action.

Chapter 2

Experimental Methodology

2.1 Overview

This chapter describes the experimental facilities, the instrumentation used to quantify the hydrodynamic forces as well as the high speed imaging system utilized for visualizing and quantifying the flow.

2.2 Experimental Facilities

The tests were accomplished in a towing tank facility of the Laboratory for Fluid-Structure Interaction (LIFE) research group within the Department of Mechanical Engineering, Universitat Rovira i Virgili. The towing tank, which was developed in 2010 consists of a carriage that can travel along a water tank of outer dimensions $0.6 \times 0.6 \times 2$ m. A variable frequency drive is used to control an AC geared motor system. The rotary motion of the motor is converted into linear motion via a belt drive system connected to the carriage. The carriage reaches a constant velocity just after the start of its motion, depending on the prescribed speed, stopped using a magnetic proximity sensor and the motion monitored by a precision rotary potentiometer.

In order to identify the operational limits of the system, a calibration process was undertaken by running the motor at different speeds to estimate the carriage linear velocities and the achievable run lengths at a steady velocity. The calibration process was conducted with increasing and decreasing input RPM to check for repeatability. Figure 2.1 presents the calibration curve. It was found that an increase in velocity results in a reduction in the run length available in order to stop the carriage safely without damaging the tank. Thus, the maximum safe achievable run lengths are restrained to around 1.45 m and velocity of 0.5 ms^{-1}.

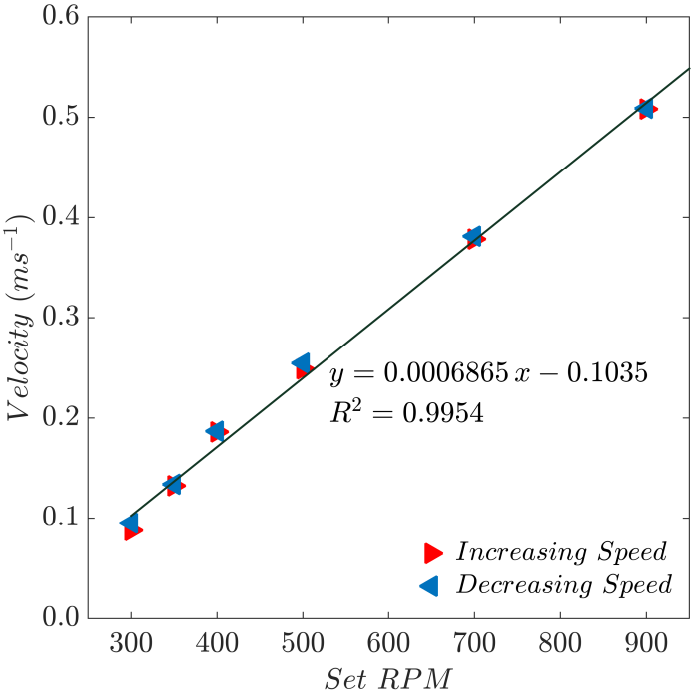

Figure 2.1: Tow tank calibration

2.3 Instrumentation

2.3.1 Force measurements

The test specimens in the tow tank were mounted by means of a L - shaped sting that was based on a vertical strut to which a submersible bending beam load cell, rated for 49 N was attached to measure the total horizontal force. The load cell was calibrated by applying a known set of weights and its voltage response measured in loading as well as unloading sequences to account for any hysteresis effects. Figure 2.2 shows the load cell response and was found to be linear.

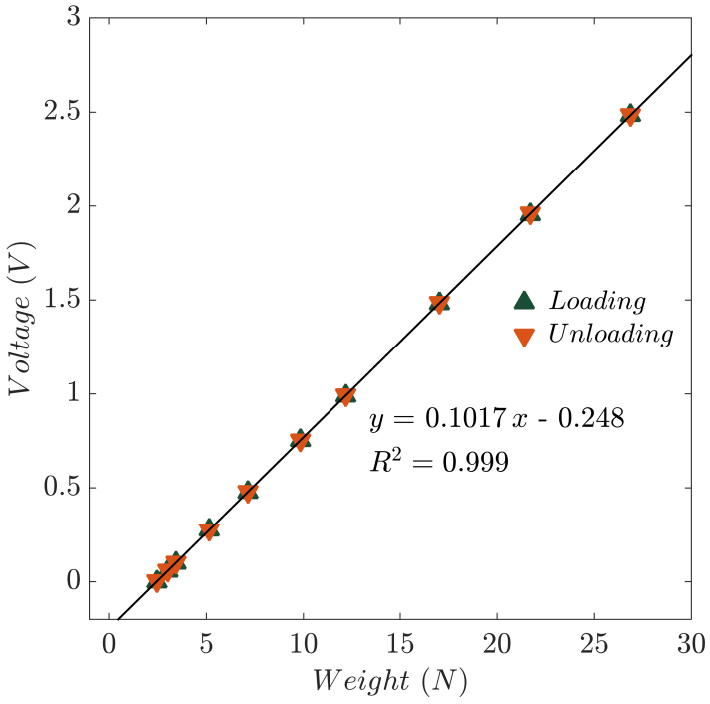

Figure 2.2: Load cell calibration

The models were connected to the load cell via a 0.25 m long screw rod, with the screw rod length being chosen to ensure minimal influence of the strut on the flow as well as yield minimum structural vibrations. The force, and the position signal from the potentiometer were sampled at 2 kHz using a data acquisition system. The lowest natural frequency of the model-sting system was identified to be near 13 Hz, well away from the frequencies excited during the experimental runs. The Cartesian coordinate system was defined such that the plate centre corresponded to the origin of the axes, with the x-axis being in the direction of tow, z-axis being in the vertical direction, and y-axis the direction perpendicular to the other 2 axes. Figure 2.3 presents a schematic of the experimental setup.

2.3.2 Qualitative flow visualization

A mixture of milk and corn-syrup was used against a dark background to visualize the flow across the rigid plates. A hollow bent steel tube of 5 mm inner diameter was mounted onto the carriage, upstream of the model and supplied the mixture continuously during the entire motion, and imaged using a high speed camera.

2.3.3 DPIV measurements

Hydrogen bubble flow technique was employed for visualizing the flow across the rigid plates. A 50 μm Nichrome wire was fastened be-

2.3 Instrumentation

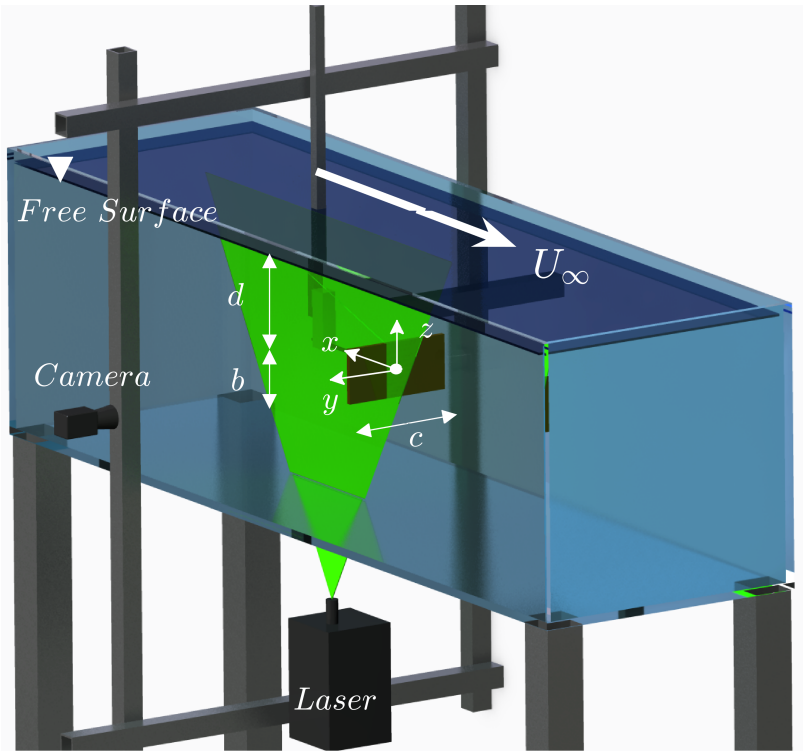

Figure 2.3: Tow tank facility with a plate specimen

tween 2 steel supports and mounted onto the carriage, upstream of the model. Power was supplied to the wire using a laboratory power supply rated 42V and 10A. Common salt was added to enhance the conductivity of water and increase the bubble concentration. A 532 nm green continuous wave laser with ancillary optics was mounted underneath the model and on the carriage to generate a laser sheet. The location of the laser sheet and the bubble wire were aligned such that most of the bubbles generated moved only in the laser sheet. The bubble-laden flow was then imaged using a 2048×1088 pixels resolution high speed camera and a 25 mm fixed focal length lens,

with the optical axis of the camera being perpendicular to the laser sheet. Image acquisition was undertaken at 170 fps and an exposure time of 1/180 s. The same setup of flow visualization was also utilized for the plates with holes and the flexible models, but with 20 μm neutrally buoyant Polyamide seeding particles in lieu of hydrogen bubbles. The acquired images were processed by intensity thresholding and the non-illuminated regions masked. PIV analysis based on Fast Fourier Transform (Willert and Gharib (1991)) was undertaken on these images using an interrogation window of 64×64 pixels and an overlap of 50% to yield 1122 and 1584 vectors in each velocity field for the experiments involving rigid plates and flexible foils, respectively. The analyses of the porous models was done with an interrogation window of 40×40 pixels and an overlap of 50% in order to capture the effect of the holes on the flow and thus yielded 4081 vectors in each velocity field. The pixel resolution was 0.25 mm, yielding spatial resolutions of 0.85 × 0.825 cm, 0.787 × 0.791 cm, 0.508 × 0.512 cm and fields of view around 28.9×27.2 cm, 49.2×26.1 cm, 51.2×27.2 cm for the rigid, flexible and porous models, respectively. The outlier vectors obtained from the cross-correlation scheme were identified after applying a threshold and replaced with new values obtained from averaging the vectors neighbouring the outlier. PIV analyses of the unperturbed flow in the absence of the model was also conducted at one of the speeds and the velocity obtained was compared against that from the potentiometer, and the error in velocity magnitude was less than 3%.

Chapter 3

Rigid flat plates

3.1 Overview

This chapter presents the methodology of data processing as well as the results of the analyses for the rigid normal plates, focusing on the effect of aspect ratio, Reynolds number, and submergence depth on the drag generated.

3.2 Experimental Setup

All the models used for the experiments in this scenario were based on the canonical profile of a plate, which was held normal to the flow. Rectangular plate models were fabricated out of acrylic sheet 5 mm thick (e). Due to the geometry, the aspect ratio of these plates was the ratio of plate span (b) to plate chord (c), and ranged from 0.25 to 4. The thickness of 5 mm ensured that no deformations took place during the experiments. Experiments were conducted at different towing speeds (U_∞), and submergence depths (d) measured from the free surface to the upper plate edge. The blockage ratio, computed as the ratio of the plate area to the tow tank cross-sectional area

was kept constant at around 8% for all cases. Table 3.1 presents the dimensions of all the models tested.

Table 3.1: Characteristics of the rigid plates

b ($\cdot 10^{-2}$ m)	c ($\cdot 10^{-2}$ m)	AR b/c	D_h ($\cdot 10^{-2}$ m)	Blockage (%)	Re_{D_h} $\cdot 10^4$
8	32	0.25	12.8	7.88	
11.5	23	0.5	15.33	8.14	
12.5	20	0.625	15.39	7.69	
14	18.5	0.756	15.94	7.97	3, 4.5, 6
15	17	0.882	15.94	7.85	
16	16	1	16	7.88	
23	11.5	2	15.33	8.14	
32	8	4	12.8	7.88	

The plates of different dimensions, as mentioned in Table 3.1 were mounted at various positions ranging from a depth such that the upper edge of the plate was located at the free surface, to a depth at which the centres of the plate and the tank were coincident. The submergence depth was always measured as the distance between the upper plate edge and free surface. The tank centre was chosen so that the upper and lower boundaries were equidistant from the plate edges and the effects on the forces generated were minimal. Each run was conducted three times to ensure repeatability of the results. Drag measurements were also conducted at the tank centre for all the speeds without the plates, to account for the forces generated by the sting and supports, which were then subtracted from the mean force to obtain the mean plate drag (F). The mean plate drag force

was then non-dimensionalized in the form of a drag coefficient (C_D) using expression,

$$C_D = \frac{F}{\frac{1}{2}\rho U_\infty^2 \, bc} \tag{3.1}$$

The expression,

$$Re_{D_h} = \frac{U_\infty D_h}{\nu} \tag{3.2}$$

$$D_h = \frac{2\,b\,c}{b+c} \tag{3.3}$$

is for the Reynolds number based on the plate hydraulic diameter.

3.3 Results

The force signals exhibit an initial acceleration peak related to added mass effect prior reaching steady state values. A second force peak is observed to exist in the latter part of the signal. This is due to the instantaneous stoppage of the carriage. In order to obtain the steady value of force generated, the accelerating and decelerating parts of the signal were not considered to avoid transient phenomena. This required the definition of specific time windows in which the analysis was conducted, ensuring only the steady part of the signals was used. The analyses windows are carriage speed dependent and during the carriage calibration trials, which involved various acceleration rates, it was found that accelerating the carriage to the steady state value within a short interval of time $\mathcal{O}$(0.1–0.6 s) ensured that a sufficient

duration of constant-velocity travel could be achieved. Thus, with the identification of the deceleration peak as the test end-point, time window sizes (in seconds) of 2.75, 2.25, 2 along with an offset of 1 s from the end-point were selected for drag coefficient computations at Re_{D_h} of $3{\cdot}10^4$, $4.5{\cdot}10^4$ and $6{\cdot}10^4$ respectively. The window sizes have been selected based on the amount of data samples available at constant travel speed. Figure 3.1 presents a typical non-dimensional force signal resulting from one of the experiments with a plate with AR of 1 at a Re_{D_h} of $6 \cdot 10^4$, at the tank centre. The time in the abscissa is in dimensionless form.

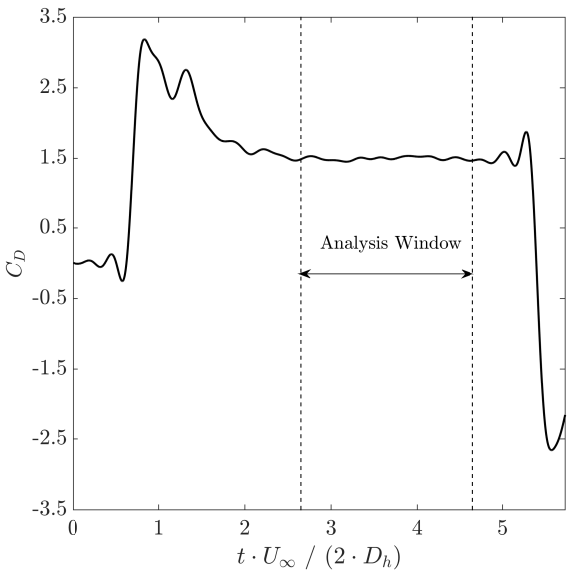

Figure 3.1: Typical dimensionless force signal for a case with $AR = 1$, $Re_{D_h} = 6 \cdot 10^4$ at the tank centre

The experiments of Fernando and Rival (2016a), Fernando and Rival (2016b) were carried out in a towing tank with plates of various

aspect ratios and they were able to observe steady drag values even when the run length was only 0.5 m. They used a dimensionless run length of approximately 5, expressed as $s^* = s/D_h$ with s being the length. With the same dimensionless expression in the experiments presented here, s^* goes up to 10.93, confirming the attainment of steady velocity and forces as in their cases.

3.3.1 Theoretical estimation

The forces involved in the problem can be estimatated theoretically by thinking of the 2D flow analysis across a normal flat plate in an infinite flow domain, using the Schwarz-Christoffel transformation (hodograph plane, Helmholtz-Kirchhoff method) (Currie, 2012) that yields the expression,

$$F_x = \frac{\pi}{\pi + 4} \rho U_\infty^2 b \tag{3.4}$$

which is developed under the assumptions of an ideal fluid with separated flow downstream of the plate such that the streamline velocity at the separation point to be that of the free-stream, and F_x corresponding to the horizontal force component. According to this equation, drag is directly proportional to the plate span. Drag estimates obtained using equation (3.4) range from 1.408 to 22.523 N, depending on the flow velocity and the plate span. The magnitude of the theoretical values for the drag are consistently higher than

those measured as expected, due to the assumptions involved in the derivation and the fact that it does not account for AR. Although limited in its applicability, the resulting values are different from the measured ones. With an AR of 0.25 and its complementary of 4, the experimental results (0.9 to 4.4 N) are close to the theoretical ones (1.408 to 5.632 N), at all speeds implying variations of 25% in C_D. This is due to the fact that this configuration can be thought to be more 'two-dimensional' compared to the other AR plates.

3.3.2 Effect of Aspect ratio on drag forces

In this section the effect of the aspect ratio is studied without taking into account the effect of the free surface, i.e. at the tank centre. Figure 3.2 presents the variation of C_D with AR for different Re_{D_h}. The plot is arranged such that ($\triangle$), ($\triangledown$), ($\square$) denote Re_{D_h} of $3{\cdot}10^4$, $4.5{\cdot}10^4$ and $6{\cdot}10^4$, respectively. At all Reynolds numbers, C_D decreases with increasing AR, with minima near $AR = 1$, followed by a monotonic increase up to the highest AR tested. The figure exhibits symmetry with respect to AR of 1 as expected, as plates with complementary AR should exhibit the same loading when not influenced by the free surface. Notwithstanding, there exists minimal differences (of approximately 3%) in the C_D magnitudes of complementary AR plates, even though the measurements have been conducted with the same plate, but rotating it 90°. The small differences are due to the fact that the tank has a finite size, resulting in some cases for the

plates to operate in closer proximity when compared to their complementary, thereby involving slightly different upper plate-edge and free surface interaction.

Although the experiments by Fernando and Rival (2016b) on various rectangular plates with AR in the range of 1 to 4 were centred on the analysis of the near wake and forces for impulsively started plates, steady drag values from their results can be inferred. In their experiments, they found square plates to have the lowest drag. This was attributed to the generation of arch-vortices from the plate edges which coalesced to form rings, and the delayed separation of the vortex rings, resulting in a greater interaction with the plate. This effect was found to be more prominent in circular plates than in square ones. The dimensionless steady force measurements on square plates (at similar Reynolds numbers) presented by the authors for AR of 1, 2, and 4, have been included in figure 3.2, showing values of C_D of 1.6, 1.75, and 1.85 for a $Re_{D_h} = 4{\cdot}10^4$, that are well in accordance to the results presented here, confirming again the measurements.

The experiments by Fage and Johansen (1927) on a floor-to-floor mounted flat plate with $AR \approx 14$ at a $Re_{D_h} = 1.5{\cdot}10^5$, yielded a C_D of 2.13 (1.86 after using blockage correction by Fail et al. (1959)), when the flow was normal to the plate. Tian et al. (2012) conducted 2D unsteady-RANS and 3D LES on case similar to Fage and Johansen (1927) and their 3D results are in good agreement with it. However, their 2D simulation results over-predicted C_D. Narasimhamurthy and

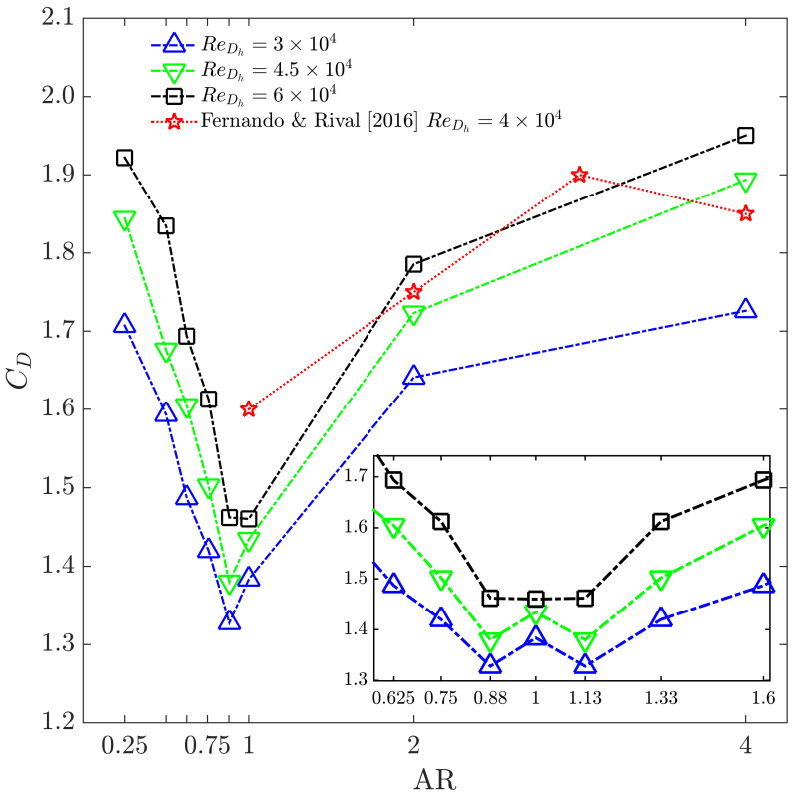

Figure 3.2: Variation of C_D with aspect ratio at different Reynolds numbers at the tank centre and inset figure highlighting the sensitive range

Andersson (2009) conducted 3D DNS studies ($Re_{D_h} \approx 0.13{\cdot}10^4$) on a setup similar to Fage and Johansen (1927), with periodic boundary condition in 1 direction and estimated the C_D to be 2.31. These results indicate the importance of 3D analyses for the flow characterization of 3D features even though the geometry is 2D.

In general, as depicted in figure 3.2, for a given Re_{D_h} C_D decreases with increasing AR, up to a minima at around $AR = 1$. Further increase in AR results in a symmetric rise. The influence of AR

reduces as it gets very small or very large, fact also observed by other researchers (Fail et al. (1959); Ringuette et al. (2007)).

3.3.3 Effect of Reynolds number on drag forces

Figure 3.2 also shows the variation of C_D with Reynolds number, with trends that are parallel to each other indicating small Reynolds number dependence if compared to that of the aspect ratio. There is the exception in the range $0.75 \leqslant AR \leqslant 1.33$, which can be observed in the inset figure. In terms of C_D magnitude, the maximum change with Re_{D_h} for a plate AR of 1 is less than 6% whereas for AR of 0.75 and 0.882, it is around 13% and 10%, respectively, indicating a larger Reynolds number sensitivity and a change in the trends shown by the curves. The C_D for the plate with AR of 0.882 is lower than that of 1 at the lowest Re_{D_h}, while the C_D magnitudes are almost equal at the highest Re_{D_h}. Fernando and Rival (2016a) showed with different elliptical plates at Re_{D_h} of the same order of magnitude, that Reynolds number sensitivity was large only when $0.67 \leqslant AR \leqslant 1.5$.

The data presented in figure 3.2 has not been blockage corrected as all the data points included were obtained as explained before, with a constant blockage. Gould (1969) developed an empirical equation based on wind tunnel tests conducted on flow across normal flat plates to understand the effect of blockage and type of mounting on the drag generated, for a fixed aspect ratio of 2. The equation for blockage corrected drag coefficient mounted centrally is of the form,

$$C_{D_c} = 1.163 \cdot (1 + 2.81 \cdot (C_D\, B) - 0.96 \cdot (C_D\, B)^2) \qquad (3.5)$$

where B denotes the model blockage ratio and C_D, C_{D_c} are the measured and corrected drag coefficients, respectively. This equation is applicable only when $0 < C_D\, B \leqslant 0.3$. Applying this correction to the values presented in figure 3.2, for the case with $AR = 0.5$ yields values of C_D near 1.6 at Re_{D_h} in the order of 10^4, which is close to the results by Gould (1969) of approximately 1.55 at Re_{D_h} in the order of 10^5. These results are comparable as well to the results by Sumner et al. (2003), involving performance quantification of kayak paddles modeled using a flat plate of $AR = 2.6$ at $Re_{D_h} \approx 3.5{\cdot}10^5$, resulting in C_D near 1.7. Although there are large differences in the Reynolds numbers of each one of these set of experiments if compared to the results reported here, they all show trends that imply the effect of Reynolds number to be limited except when aspect ratios are near 1.

3.3.4 Effect of submergence depth on drag forces

In this section the effect of the proximity to the free surface is investigated, the highlight of this study. Figure 3.3 presents the variation of drag coefficient for all the plates, with non-dimensional depth to chord ratio, at all the Reynolds numbers and aspect ratios investigated. In all the horizontal axes, the largest depth corresponds to the tank centre position, so in this configuration it was ensured that

the free surface and the lower wall of the tank were equidistant from the plate edges. Again, a $d/c = 0$ means that the upper edge of the plate is located at free surface at the start of experiment.

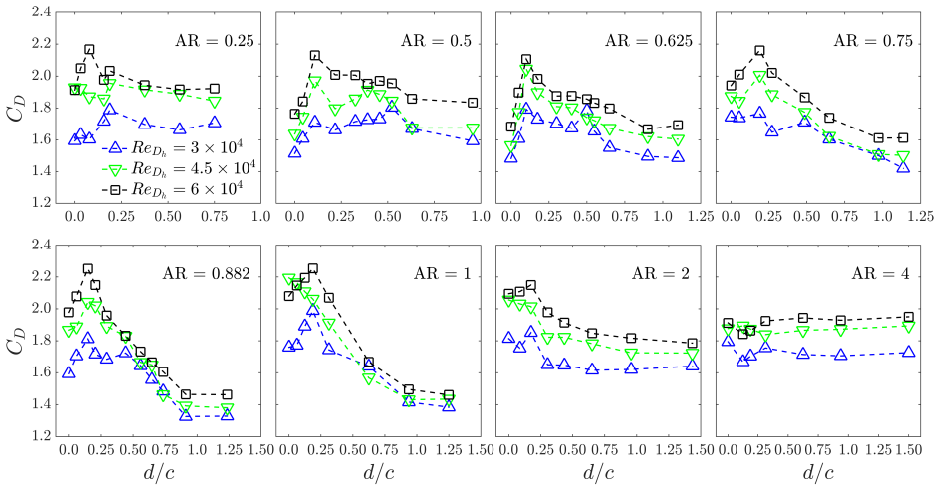

Figure 3.3: Variation of drag coefficient with depth-chord ratio at the three Reynolds numbers investigated

An increase in submergence depth from the free surface, results in an abrupt increase in drag coefficient, peaking at a $d/c \sim 0.1$ followed with a reduction that leads to the values measured at the tank centre. This is true for plates of $AR < 0.75$, whilst plates with AR of 0.75, 0.882, 1, and 2, the peak is attained at $d/c \sim 0.2$. The trends for the case of AR of 4, indicate a limited effect of the free surface on the generated drag force, as expected. Overall, all the plates apart from AR of 4, present a monotonic increase in drag force followed with an abrupt drop as the submergence depth is reduced from the tank centre to the free surface. It is also observed that the sudden drop in drag at the free surface for AR of 2 from a d/c around 0.2 is not as

prominent as that observed on AR of 0.5 from d/c approximately 0.1. The absence of variation in drag force with submergence depth for the plate with AR of 4 is opposite to that observed in its complementary configuration. These show the decreasing influence of aspect ratio on drag force with increasing depth, indicating that the effect of AR is limited after a critical value, confirming the results of other researchers (Ringuette et al. (2007), Fernando and Rival (2016a)).

Figure 3.4 presents the same data, but now the depth has been non-dimensionalized using the hydraulic diameter, for plates of AR ranging from 0.5 to 2, as they have comparable magnitudes of hydraulic diameter. The primary drag peak takes place now at a $d/D_h \sim 0.2$ in all cases.

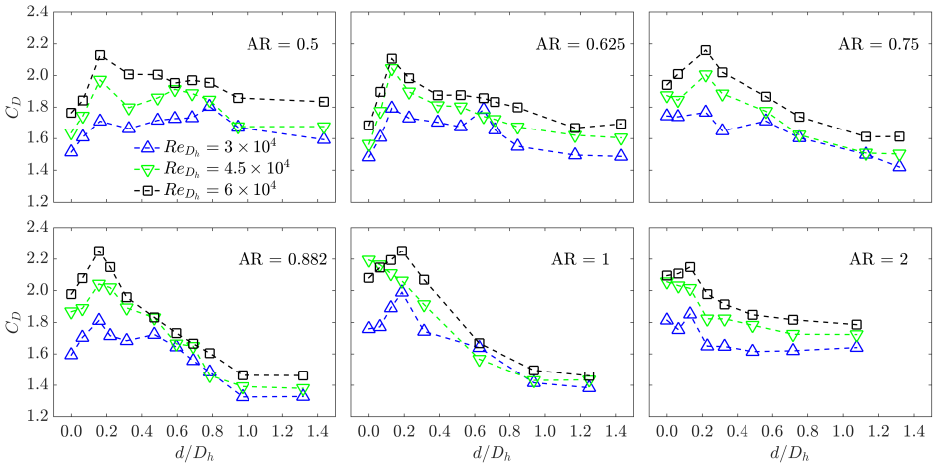

Figure 3.4: Variation of drag forces with depth-hydraulic diameter ratio at the three Reynolds numbers investigated

Arslan et al. (2013) studied the effect of free surface on a rectangular cylinder spanning their entire test-section (with a 10% blockage) at

different submergence depths and Re_{D_h} near $1.8{\cdot}10^4$. Their numerical and experimental results showed a $C_D \approx 1.8$ for a rectangular cylinder of $AR \approx 0.2$ when near the free surface. The result of $C_D \approx 1.6$ for AR of 0.25 and Re_{D_h} of $3 \cdot 10^4$ at a position similar with respect to the free surface is comparable, considering the fact that the flow around a non-circular cylinder differs to that over a flat plate. Similarly, the C_D results of Malavasi and Guadagnini (2007) (case (b)) are well within the measurement band for plate AR of 0.25. The 2D RANS results from Liu et al. (2016) indicate the presence of a recirculation zone in the plate downstream when operating in close proximity to the free surface, with size varying inversely with depth. These simulations however did not account for the plate orientation or the mutual interaction of the vortex structures forming at the other edges which result in a smaller wake.

With the free surface being a deformable boundary, Froude number is another parameter that can be used for studying the drag of the plates, apart from depth ratio. Here, the characteristic length used for Froude number computation is the submergence depth. Bouscasse et al. (2017) included in their work a discussion on the different possibilities of characteristic lengths when studying the flow around a cylinder near the free surface. Thus, the magnitude of Froude numbers ranges from 0.13 when the plate is located at the tank centre to a value of around 1.2 when the upper plate edge is located near the free surface to finally reaching an extremely high value at free surface. Figure 3.5 presents this variation for all the plates tested. Similar to

figure 3.3, it can be seen that no trends are visible for plate AR of 4 at any of the tested Re_{D_h} whereas the rest of the plates present a peak in drag. The location of the drag peak also shifts rightward to higher Fr_d, with increasing Re_{D_h}, from $Fr_d \sim 0.4$ to $Fr_d \sim 0.8$.

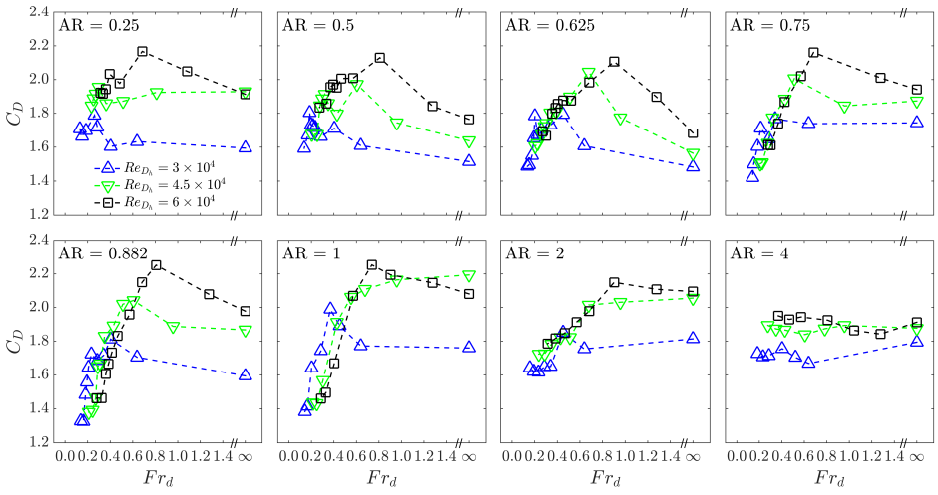

Figure 3.5: Variation of drag forces with Froude number for different plates at the three Reynolds numbers investigated

Besides force measurements, the results of qualitative flow visualization at Re_{D_h} of $4.5{\cdot}10^4$ using milk indicated the change in the wake characteristics and thus was the motivation for further analysis using the PIV technique. Figure 3.6 presents the results of flow visualization and can be seen that an asymmetric wake exists at low submergence depth, unlike in the other cases.

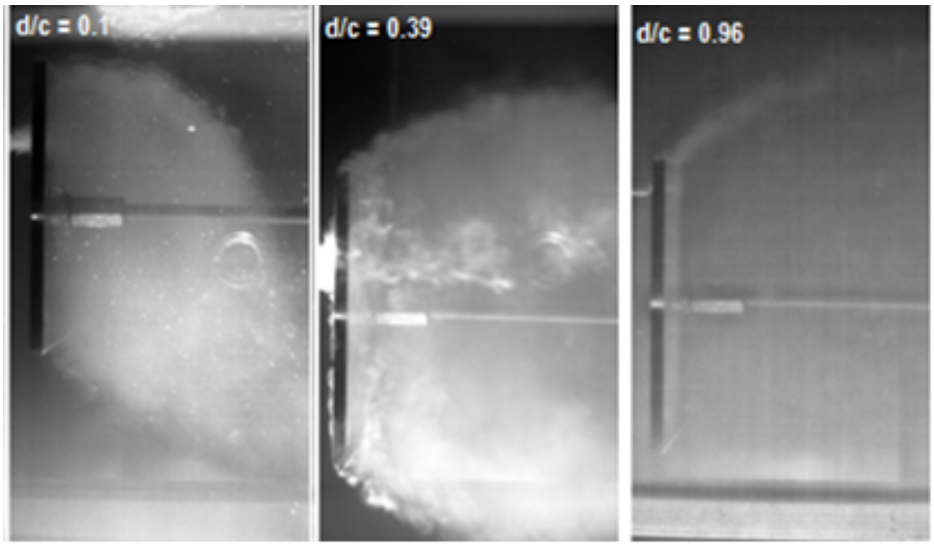

Figure 3.6: Variation in wake profiles at specific submergence depths for $AR = 0.5$

3.3.5 Wake characterization

In this section results obtained by means of PIV show the evolution of the near wake region of the plate. In figure 3.7, the flow fields resulting from PIV interrogations carried out at 6 specific depths with the plate of $AR = 0.5$, are depicted. This data was obtained at a Re_{D_h} of $4.5 \cdot 10^4$, and in the figure the flow is from left to right. The images have been ordered with increasing depth, starting from the free surface ($d/c = 0$) in the upper row of plots, to the tank centre ($d/c = 0.96$). The colour map indicates the sign of the vorticity field with red for clockwise and blue for counter-clockwise directions. The thick black vertical line is used to indicate the location of the plate, while the thick blue lines are used to indicate the approximate lo-

cation of the free surface. The free surface distortion was estimated from the PIV images using an in-house image processing code. The location of the sting has not been included here for the sake of clarity, but as described in the experimental set-up, it was connected at the middle of all the plates investigated. The three vorticity fields shown at each depth correspond to time averaged fields over a Δt of 0.25 s. The first 2 fields at every depth (in the first two columns) correspond to the initial wake formation phase and have been included in order to see the evolution of the wake up to the steady part of the run and for validation with other researchers findings, even though the drag analysis presented in the previous sections, has been carried out only with the steady part of the run, as explained before (third column). The non-dimensional time indicated per column (t^*) is defined based on the timing of last vorticity field utilized for averaging the specific band to the total run-time, and the vorticity has been non-dimensionalized using the hydraulic diameter and the towing speed.

3.3 Results

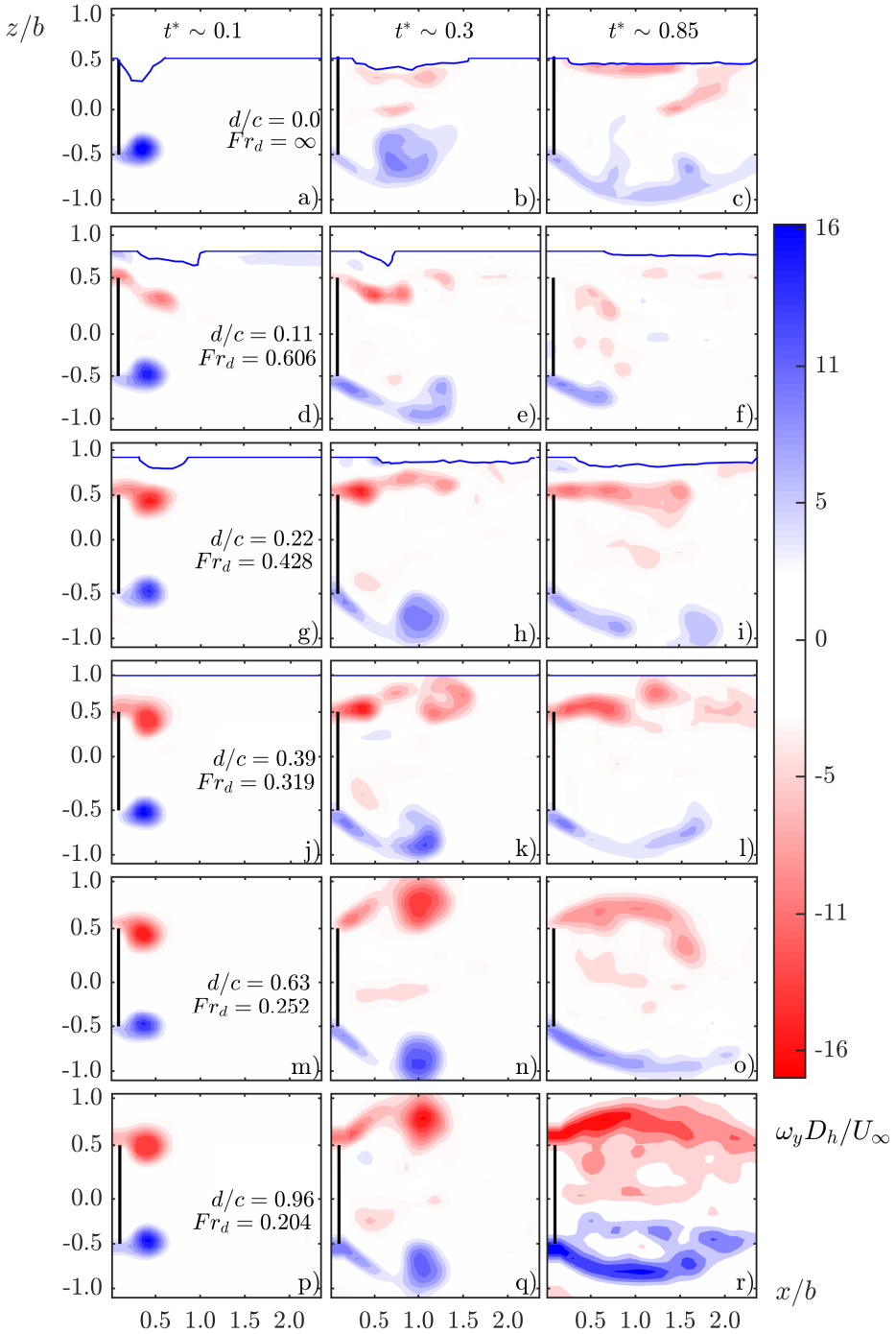

Figure 3.7: Near wake evolution for $AR = 0.5$ plate at different instants of time and depths, at $Re_{D_h} = 4.5 \cdot 10^4$

At the tank centre ($d/c = 0.96$) in the last row, the initiation of the plate motion (plot 3.7p) results in the generation of vorticity at the edges. The vortices evolve and travel downstream as the plate accelerates, with the vorticity being fed continuously through the shear layers connected to the plate edges (plot 3.7q). When the plate achieves a constant velocity (plot 3.7r), the initial vortices are shed and a newer set of vortices are produced which in the averaged vorticity field has the form of an elongated shear layer, with reverse flow occurring at the mid-span location. The symmetrical arrangement of the initial vortices and the shear layers about the $z = 0$ plane indicate minimal influence of the boundaries on the wake. This begins to change as the depth is reduced. At $d/c = 0.63$ (plots 3.7m-3.7o), the initial evolution and the lower shear layer appear similar to that at the tank centre but the free surface starts to have an influence on the upper shear layer. Further reduction in depth depicts drastic differences with the loss of wake symmetry being the most observable feature. At d/c of 0.39 (plots 3.7j-3.7l) and 0.22 (plots 3.7g-3.7i), the lower shear layer evolution is still close to that observed at the tank centre while the upper shear layer is affected by the free surface significantly due to increasing interaction between the gap-flow and free surface. When the depth is $d/c = 0.1$ (plots 3.7d-3.7f), neither the initial vortices nor the steady state flow are comparable to that at the tank centre. The flow occurring in the gap between the free surface and the upper plate-edge at this depth interacts with the free surface resulting in the vortex formed at the upper plate edge to evolve

closer to the plate and towards the midspan region compared to that at the other edge. The free surface modifies the vortex formation on both the edges, but effects are obviously stronger on the upper edge. By the time the plate has achieved constant velocity, the interaction of the upper vortex with the free surface results in the shear layer being bent downwards and towards the opposite edge. This results in a significant recirculating flow that envelops the base region of the plate. Conversely, at d/c of 0 (plots 3.7a-3.7c), no such interactions are visible due to the fact that there exists no gap-flow above the upper plate edge. The flow across the lower plate edge is similar to that observed at the tank centre. Within these plots, the free surface distortion is visible only up to a d/c of 0.22. By the time the steady flow is attained, the free surface is disturbed and lie at a level below compared to that at the start of the experiment.

PIV measurements were also conducted with the plate AR of 0.25, with the results presented in Figure 3.8. The flow at d/c of 0.75 (plots 3.8g-3.8i) is very similar to that of $AR = 0.5$ at d/c of 0.96 (plots 3.7p-3.7r), which reinforces the argument of minimal interference of the boundaries. At d/c of 0.08 (plots 3.8a-3.8c), the gap-flow interacts further downstream ($x/b \sim 1.7$) of the plate than in the case with AR = 0.5 at d/c of 0.1 ($x/b \sim 0.9$), and the upper shear layer evolution is such that there exists no significant recirculating flow on the base region of the plate. At d/c of 0.1875 (plots 3.8d-3.8f), the visualized gap-flow is in an intermediate state to that observed at d/c of 0.22 and 0.39 for the plate AR of 0.5.

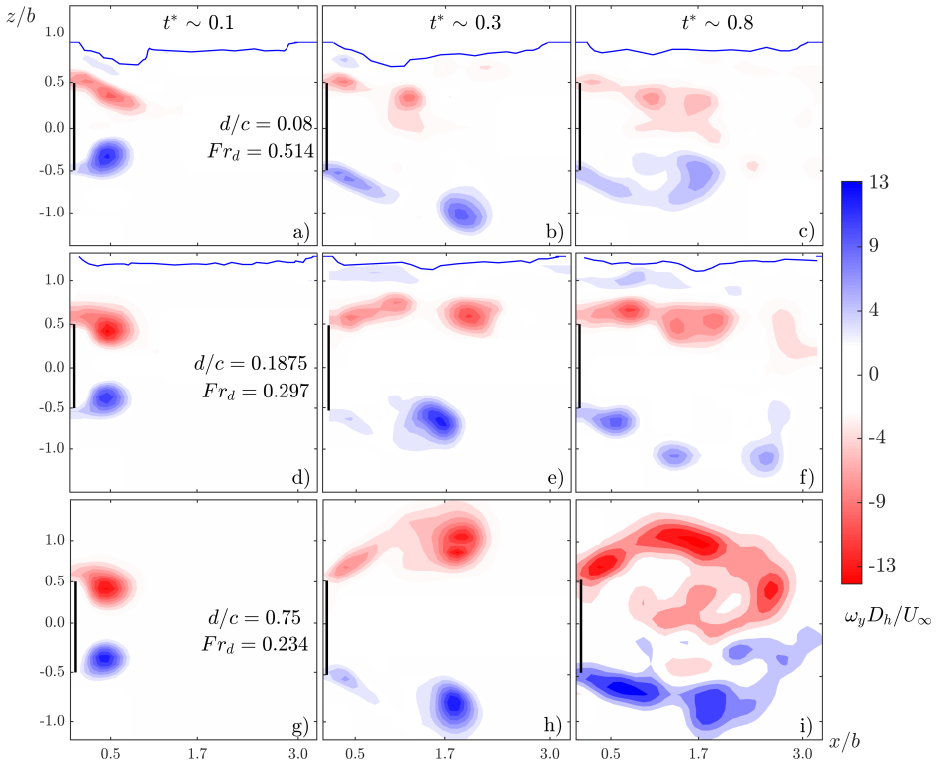

Figure 3.8: Near wake evolution for $AR = 0.25$ plate at different instants of time and depths, at $Re_{D_h} = 4.5 \cdot 10^4$

3.4 Discussion and Remarks

The force measurements and flow visualization have provided crucial information regarding the behaviour of plates of various aspect ratios when being towed both near and far from the free surface. Far from any of the boundaries, vortices are shed from the plates in a symmetric manner during the acceleration phase, with another set of vortices from plate forming the visualized shear layer. The process of shedding of the initial vortices, with the production of newer

vortices from plate edges has also been observed by Fernando and Rival (2016b) on plates of aspect ratios in the range from 1 to 4, who denoted them as primary and secondary vortices, respectively. They also linked the evolution of these vortices to the crests observed in their C_D temporal plots. Not only do their flow visualization results match well with present results when comparing the initial phase of the experiments, but also their steady drag data matches well when compared to the data, as commented in the previous sections.

The variation of submergence depth introduces new interesting phenomena and large changes in the drag forces observed, not reported before. In section 3.3.4 it was shown how a drag peak appears at $d/c \sim 0.1$ for AR of 0.25 to 0.625 which shifted to $d/c \sim 0.2$ in the rest of plates, to its final disappearance for the $AR = 4$ case. The absence of variations in drag when submergence depth was varied, in the case with the plate AR of 4, indicates the minimal effect of the shear layer structures that develop parallel to the free surface. Figure 3.3 showed how for the specific case of AR of 0.5, for which the PIV data appears in figure 3.7, the C_D value increased somewhere between a 12% to a 20% (depending on Reynolds number), as submergence was changed from the free surface to the drag peak location. After the peak, C_D reduces monotonically to the values at the tank centre. The location of the peak for the case with AR of 0.25 appears to be dependent on Reynolds number. For this case, the PIV data in figure 3.8, at d/c of 0.08 and Re_{D_h} of $4.5 \cdot 10^4$ shows no strong recirculating flow enveloping the base region of the plate, un-

like the case of the plate with AR of 0.5 at the same Re_{D_h}. The PIV data in figure 3.7, indicates that this peak is due to the existence of a strong recirculating flow in the base region. For most of the plates, the observation of abrupt rise in drag followed with a reduction holds true even while using D_h for non-dimensionalization of submergence depth, with the results presenting a collapse of the data for all the plates and the drag peak occurring approximately at d/D_h of 0.2.

Miyata et al. (1990) as well as Liu et al. (2016) have observed a similar recirculating flow caused by a biased gap-flow, in their studies with a cylinder and a flat plate at different submergence depths, respectively. However, the results from Miyata et al. (1990) indicated a very different drag force that changed abruptly on their cylinder, with drag being lower at low submergence depths, if compared to the data presented here. The 2D simulations from Liu et al. (2016) have captured this flow feature, but neither the C_D magnitudes nor the trends are in agreement with the current results. The differences can be attributed to the fact that the wake generation process for a plate is inherently three dimensional at all submergence depths.

In terms of Froude numbers, it was observed that an increase in Re_{D_h} resulted in translation of the drag peak location to higher Fr_d. Reichl, P., Hourigan, K., Thompson (2005) presented in detail the flow structures and wake interactions from 2D simulations of a cylinder at various Froude numbers and depth ratios, at low Re. They indicate that vortex shedding for a cylinder ceases to exist when the

depth ratio is less than approximately 0.3 and Froude numbers are between 0.25 and 0.4. This is due to the interaction of the vortex from the top half of the cylinder with the free surface and resulting in free surface distortion and introduction of vorticity of strength opposite to that shed from the lower half of the cylinder and annihilating it. However, it must be mentioned that the characteristic length utilized by them was the cylinder diameter. Choosing submergence depth as characteristic length for Froude number results in a relation $Fr_d = Fr_D/\sqrt{\frac{d}{D}}$, indicating an inverse relation between critical Froude number and depth ratio, ranging from 0.4 to 0.63 for fixed depth ratio of 0.4. This indicates that in order for a cylinder to continuously shed vortices even at lower depth ratios, the Froude number has to be increased. Bouscasse et al. (2017) has also found similar results from his simulations. The force and PIV results for AR of 0.5 show a drag peak, and substantial reduction in the length of the wake structure when $d/c \approx 0.1$ and $Fr_d \approx 0.6$, respectively. This indicates that plates have a similar dependency.

Far from the free surface, the flow separation occurring at the plate edges and the resulting low base pressure is the major source of drag. Near the surface, drag is expected to increase due to wave formation, with increasing significance with increasing Reynolds and Froude numbers. At a given Reynolds number, it is known that the reduction in submergence depth creates divergent and transverse surface waves which alter the wake characteristics and thereby the force generated. The results from experiments of Benusiglio et al. (2015)

showed that the ratio wave drag to total drag, on spheres under the influence of the free surface changes quickly with submergence depth.

On the whole, the drag forces showed minimum values for aspect ratios close to 1 when plates are away from the free surface, with the trends also being insensitive to changes in Reynolds number, except when $0.75 \leqslant AR \leqslant 1.33$. However, the trends with changing submergence depth were observed to be clearly dependent on Reynolds number, and on aspect ratio to a smaller extent. Most of the plates presented an increase in drag at low submergence depths, with hydraulic diameter acting as a good parameter for non-dimensionalization. The peak in drag has been linked to the interaction between the free surface, the resultant gap-flow and the upper shear layer. This interaction leads to the formation of a recirculating flow in close proximity to the base region of the plate, due to the ability of free surface to distort and enable fluid entrainment.

Chapter 4

Flexible foils

4.1 Overview

This chapter presents the methodology of data processing as well as the results of the analyses for flexible normal foils, with the focus of the study being the effect of flexibility and submergence depth on the drag generated.

4.2 Experimental Setup

In this scenario, the material as well as thickness was varied in order to achieve a spectrum of flexibilities, measured as a product of E and I, but with the aspect ratio fixed at 0.625. The results obtained from the rigid case were used as a benchmark to compare the behavior of the flexible models, owing to the fact that its deflection under fluid loading is negligible. Foils of different thickness, ranging 25-125 μm but with same AR as the acrylic case were fabricated of brass, steel or Polyethylene Terephthalate (PET) to obtain different values of flexural rigidities, which allowed for the calculation of Cauchy numbers (C_Y). The flexible models were fabricated by attaching the foils us-

ing cyanoacrylate based adhesive onto a small acrylic skeleton with a span of 2.5 cm and chord equal to that of the acrylic plate, which resulted in the length of the flexible region (l) to be 5 cm on either side of the skeleton, and was kept constant for all the cases. The blockage ratio was the same as before, around 8% for the rigid case. With the towing velocity and the cantilever length being constant, thickness plays a major role in controlling the flexural rigidity due to its relationship with the sectional moment of inertia being cubic in nature. Thus, large changes in Cauchy numbers have been achieved by varying the foil thickness marginally.

Table 4.1: Characteristics of the flexible models

Case	**Material**	$\boldsymbol{e}$ $\cdot 10^{-6}$ **m**	$\boldsymbol{E}$ **GPa**	$\boldsymbol{C_Y}$
1	Acrylic	5000	3.2	0.0003
2	Brass	100	100	1.1
3	Brass	75	100	2.6
4	Steel	50	210	4.1
5	PET	125	5	11
6	Steel	25	210	33
7	PET	50	5	173

Table 4.1 presents a summary with the main characteristics of the tested models, such as material, thickness, Young's modulus (E), Cauchy number, at a chord-based Reynolds number of $6{\times}10^4$. The models were mounted as before, at various positions ranging from a depth such that the undeflected upper edge of the foil was located at the free surface, to a depth at which the centres of the foil and

the tank were coincident. The submergence depth was always measured as the distance between the upper edge of the foil and free surface. Each run was repeated five times to ensure repeatability. Base drag measurement, that is a run without the model was also conducted at the tank centre to account for the forces generated by the sting and supports, which was subtracted from the mean force to obtain the mean plate drag ($\overline{F}$). The mean plate drag force was then non-dimensionalized in the form of a drag coefficient (C_D) using expression,

$$C_D = \frac{\overline{F}}{\frac{1}{2}\rho U_\infty^2 bc} \tag{4.1}$$

The Cauchy number is calculated using the expression,

$$C_Y = \frac{\rho U_\infty^2 \, c \, l^3 \, C_{D_0}}{2 \, EI} \tag{4.2}$$

where I the sectional moment of inertia of the model, $\frac{c\,e^3}{12}$, and C_{D_0} is the drag coefficient of the rigid plate at the tank centre.

4.3 Results

Similar to the results observed in the previous chapter, the force signals exhibit 2 prominent force peaks- an initial acceleration peak related to added mass effect prior reaching steady state values and

another in the latter part of the signal due to the instantaneous stoppage of the carriage. For steady force calculation, it is essential to disregard the regions of transient phenomena and requires usage of specific analyses windows. Thus, within these sets of experiments,

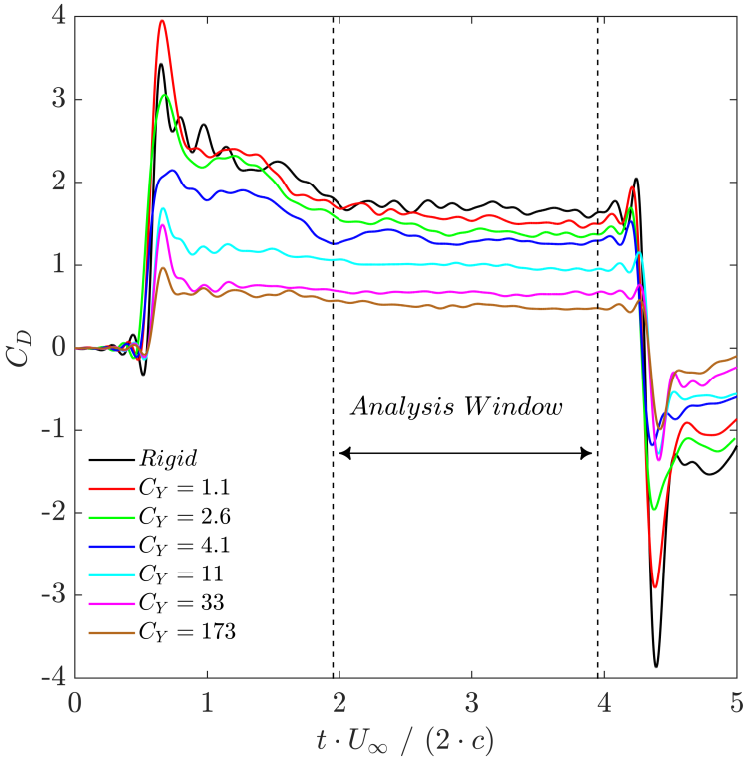

Figure 4.1: Typical non-dimensionalized force signal for all the models at the tank centre over a single run

the time window size of around 2 seconds along with an offset of 0.5 s from the end-point were selected for drag coefficient calculations. Figure 4.1 presents a typical non-dimensional force signal resulting from one of the experiments for each of the models at Re_c of $6{\cdot}10^4$, at the tank centre against non-dimensional time. s^* in these experi-

ments goes up to approximately 12 for certain flexible models, which indicates the attainment of steady velocity and forces as in cases of Fernando and Rival (2016a,b), while figure 4.2 is a representative montage of the attained foil deflection during the steady state.

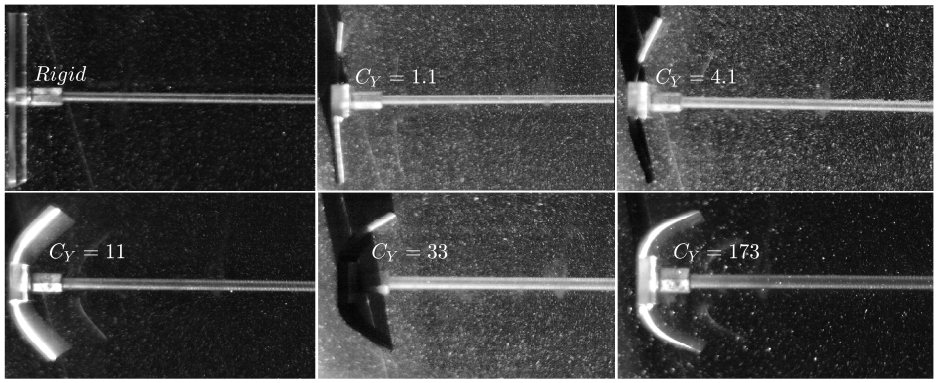

Figure 4.2: Snapshot of steady state deflections for the specified models at tank centre

4.3.1 Effect of Flexibility on drag forces

In this section, the variation of drag coefficient with flexibility is discussed for all models when operating at the tank centre that is, far from the lower boundary as well as the free surface. With the aspect ratio, towing velocity and the cantilever length being the same for all the cases, Cauchy number is dependent only on EI, the flexural rigidity. The lowest Cauchy number corresponds to the completely rigid acrylic plate and the highest to the 50 μm PET foil, the most flexible case. Figure 4.3a presents the variation of drag coefficient with C_Y whereas Figure 4.3b the variation of Reconfiguration num-

ber, defined as the ratio of the measured force to that experienced by the most rigid plate ($\Re = \frac{\overline{F}}{\overline{F}_R}$), when located far from any of the boundaries. Here $\overline{F}_R$ corresponds to the force experienced by the acrylic plate. From figure 4.3, it can be seen that the drag coefficient as well as $\Re$ decreases with increasing C_Y. The drag coefficient of the rigid plate is around 1.6 and begins to decrease as the Cauchy number starts to increase, with the drop in C_D being significant even at Cauchy numbers as low as 2.6, as expected due to the reduction in the exposed or frontal area. Further increase in Cauchy numbers only enhances this drop in drag, with the value for the most flexible case tending to approximately a quarter of that experienced by the rigid plate. Figure 4.3b presents same phenomena with the Reconfiguration number. Results obtained by other researchers (Gosselin et al. (2010); Leclercq and de Langre (2016)) have also been plotted for comparision and it can be observed that there is a very good match with the published results over the range of C_Y tested, confirming the reconfiguration process to be mostly two-dimensional in this case too.

The steady drag results from Fernando and Rival (2016a) for an elliptical flat plate with an aspect ratio of 1.5 and Re_{D_h} of $5{\cdot}10^4$ is around 1.5, which is close to the value obtained by us for the plate with highest rigidity. The current result is comparable with the former due to the effect of edge discontinuities on drag being minimal (Fernando and Rival (2016b)), and that the orientation of the rectangular plate has an insignificant effect on the drag generated when

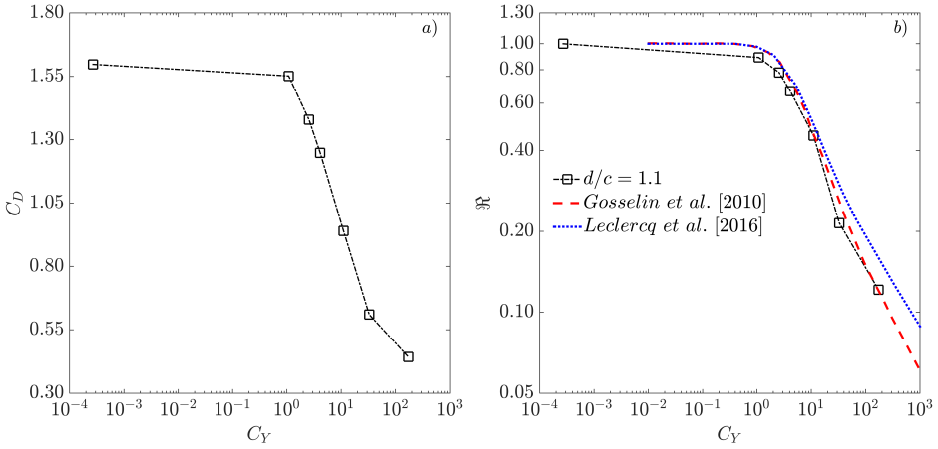

Figure 4.3: Variation of drag coefficient and Reconfiguration number with Cauchy number

located far from any of the boundaries, at a given aspect ratio (AR = b/c or c/b). Overall, the current results are in good agreement with those presented by other authors, thus confirming the measurements as well as the methodology of analysis.

4.3.2 Effect of submergence depth on drag forces

In this section, the effect of the proximity to free surface is studied for all the models with the aforementioned Cauchy numbers. Again, the submergence depth has been measured as the distance between the free surface and the undeflected upper edge of the foil. This value in turn, has been non-dimensionalized using the plate chord. Thus, $d/c = 0$ corresponds to the case with the upper edge at the free surface, and $d/c = 1.1$ to the scenario when the model edges are equidistant from the free surface and the bottom wall.

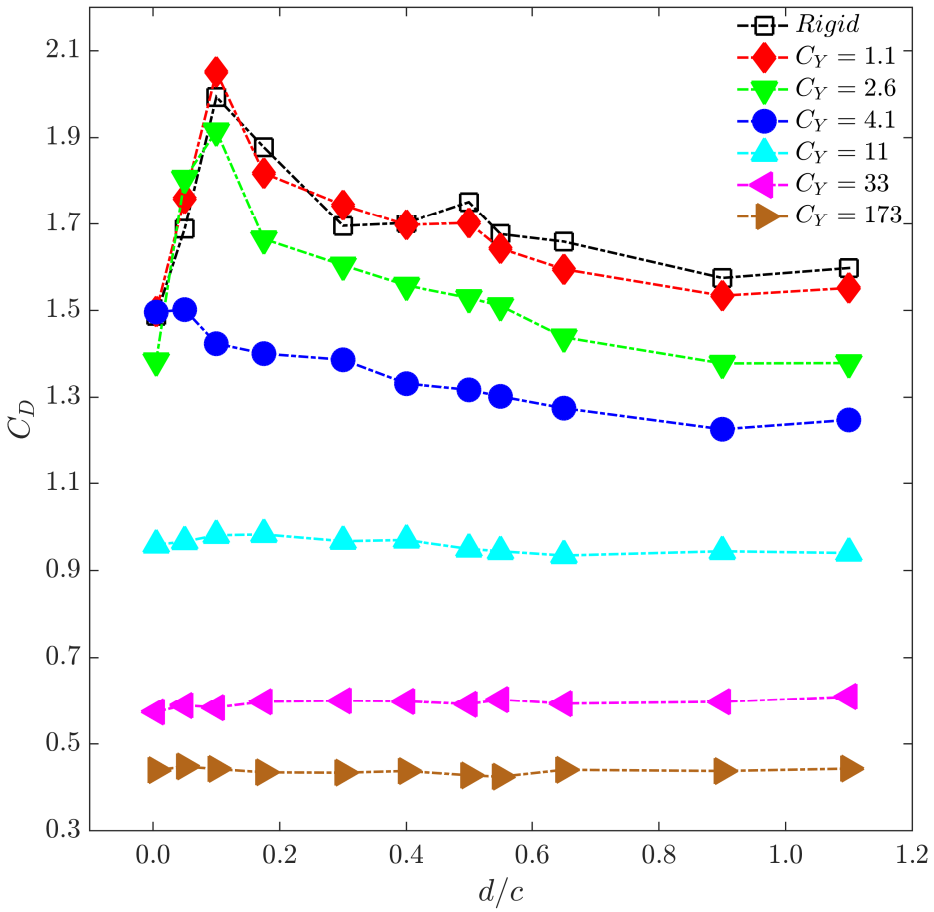

Figure 4.4: Variation of drag coefficient with depth ratio for models at different Cauchy numbers

Figure 4.4 presents a variation of drag with depth, with the solid symbols representing the flexible cases and (□) the rigid plate. For the rigid case, C_D monotonically increases as the submergence depth is reduced from tank centre to $d/c \sim 0.1$, followed with an abrupt drop in values as the submergence depth is further reduced to zero, as indicated in chapter 3. This behavior is also replicated for C_Y values

up to 2.6, however the drag values at tank centre are correspondingly lower, as has been explained in the previous section. At C_Y of 4.1, C_D values appear to monotonically increase till the free surface with the abrupt increase in drag being conspicuously absent. For $C_Y \geqslant 11$, drag coefficient presents no such variation with depth, indicating that the generated drag force to be independent of submergence depth. It must be restated that the drag coefficient calculations presented here have been done using the frontal area of the rigid plate as the reference area for all the cases.

Previously, chord as well as hydraulic diameter was used for non-dimensionalization of submergence depth and the latter was found to be a good parameter which resulted in the drag peak to be located at approximately $d/D_h \approx 0.2$ for most of the plates. However, with the current experiments involving flexible structures and the consequent area reduction, hydraulic diameter changes with flexibility. Thus, chord is the only parameter that remains constant for all the models and is better suited as a reference.

4.3.3 Foil deflection estimation

In this section, an estimate of the maximum foil deflection and tip location is attempted using Euler-Bernoulli beam theory (Timoshenko (1983)). From theory, it is known that a cantilever beam subjected to an uniformly distributed load (q Nm^{-1}) about its length l undergoes a deflection of the form,

$$u(z) = \frac{q}{24\,EI}(z^4 - 4l\,z^3 + 6l^2\,z^2) \tag{4.3}$$

where z is the coordinate along the beam length, u the deflection and x the direction of loading. The loading on the cantilevered sections has been calculated by subtracting the force acting on the region of the skeleton from the total drag. The drag on the skeleton region has been estimated in turn using the drag value obtained on the rigid plate at the tank centre and assumed to be distributed uniformly along its span. The deflection estimate from this equation can be observed in Figure 4.5a where the dotted lines correspond to theory, the points (♦, ●, ▲, ◀, ▶) to the actual tip location obtained from the captured images, and the solid black line to the rigid plate location. It can be observed in figure 4.5a that the theoretical estimates are close to the experimental values for cases up to C_Y of 4.1. This indicates that the linear theory is valid and can be utilized for estimating the foil tip position due to the deflections being not very strong. However, the deviation from theory increases with increasing C_Y. It is interesting to note that the theoretical deflection at C_Y of 173 is higher than the actual deflection, whereas it is the opposite when C_Y is 11 and 33. This suggests at a deflection limit or the existence of a 'universal' shape that is achieved when the trailing edges are parallel to the flow, and the classical beam theory is valid when the Cauchy numbers are mild and the model is far from any of the boundaries.

Figure 4.5b presents a similar analysis at specific submergence depths

4.3 Results

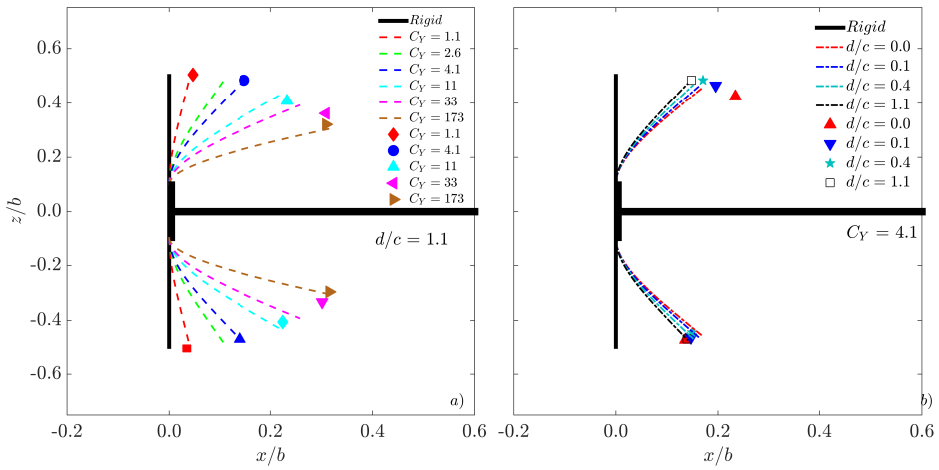

Figure 4.5: Variation of foil deflection with Cauchy numbers and depth ratio

where images have been acquired for the case of C_Y of 4.1, which has been chosen specifically due to the very good match observed between theory and experiments in figure 4.5a. It can be seen that at high submergence depths the agreement between theory and experiments is very good, with the difference being less than 2%. However, the match between theory and experiments changes with submergence depth. The differences are more significant on the region closer to the free surface than the lower edge. On the lower side, the foil is seen to maintain a similar position experimentally at all the visualized depths, indicating similar or no effect of free surface on the deflection. The deviation from theory increases with reducing depth as expected due to the greater proximity of the upper edge of the foil to free surface when compared to the lower edge. These results prove that the assumption of an uniformly distributed load in linear beam

theory cannot be expected to provide accurate information regarding foil deflection when in proximity to the free surface or when the deflections are extremely large.

Even though the linear beam theory is limited to small deflections, its simplistic formulation and applicability to a vast range of problems renders it extremely convenient. In order to obtain a better estimate of large deflections at high C_Y values and different submergence depths, the loading has been assumed to be varying along the span and is of the form,

$$q = q_0\left(1 - \frac{z}{l}\right)^n \tag{4.4}$$

where n is the loading exponent, with n equal to 0 corresponding to the classical uniform distribution (UDL), a constant load and n of 1 to a uniformly varying load (UVL) with the force magnitude being maximum at $z = 0$ and zero at $z = l$. Substituting this form of loading into the beam equation and the implementation of the appropriate boundary conditions for a cantilever with one end rigidly mounted and the other end being free yields,

4.3 Results

$$EI\frac{\partial^4 u}{\partial z^4} = q_0\left(1-\frac{z}{l}\right)^n \tag{4.5}$$

$$u = \frac{q_0 l^4}{EI(n+1)(n+2)(n+3)(n+4)}\mathcal{Z} \tag{4.6}$$

$$\mathcal{Z} = \left[\left(1-\frac{z}{l}\right)^{n+4} - \left(1-\frac{z}{l}\right)(n+4) + (n+3)\right] \tag{4.7}$$

And the equation for maximum tip deflection being,

$$u_{max} = \frac{q_0 l^4}{EI(n+1)(n+2)(n+4)} \tag{4.8}$$

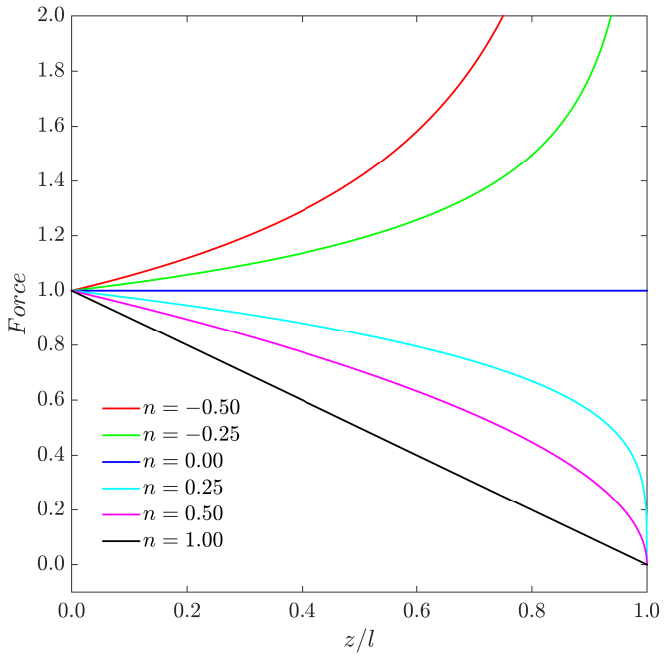

Figure 4.6: Cantilever load distribution at different loading exponents

Substituting the values of n being equal to 0 or 1 yields the maximum tip deflection of $\frac{q_0 l^4}{8EI}$ and $\frac{q_0 l^4}{30EI}$, which correspond to the conditions of UDL and UVL, respectively. Figure 4.6 presents the load distribution for specific loading exponents. When equation 4.8 is utilized for identifying the loading exponents in the experiments at tank centre, they are obtained as $\sim$ [0.175,-,0,-0.075,-0.25,0.213] for the Cauchy numbers ranging from 1 to 173, respectively. Due to the fact that imaging was not undertaken at C_Y of 2.6, no exponent has been identified. An exponent rated $0 < n < 1$ signifies a loading of a form intermediate to UDL and UVL, wherein the force acting along the cantilever length is reducing at a non-linear rate, but with the force acting at the tip to be zero, whereas a negative exponent signifies a loading which reaches infinite values at the tip. The magnitude of the exponents also indicate the same– that the UDL assumption is valid for low to medium C_Y values, post which the exponent becomes negative indicating that the loading needs to account for an extra force that acts near the tip which results in a greater deflection. At higher C_Y, the exponent is positive again, indicating that the loading is again non-linear but such that the tip load is zero. A relation between the loading exponent and Cauchy number is obtained by curve fit and is of form,

$$n = -0.1505 \ln(C_Y) + 2.165 \cdot 10^{-5} (C_Y)^2 + 3.27 \cdot 10^{-4} (C_Y) + 0.249 \quad (4.9)$$

4.3.4 Reconfiguration number and Vogel exponent

In this section, the effect of reconfiguration is presented in greater detail. For the sake of brevity, Figure 4.7a presents the variation of Reconfiguration number with Cauchy number only for certain depths, where $\Re$ has been defined as the ratio of the force experienced by a foil at a particular depth to that of the rigid plate of the same AR at tank centre. From this figure, it can be observed that an increase in Cauchy number results in reduction in magnitude of $\Re$, indicating that the drag generated by the foil to be lower than the plate. Except for varying magnitudes, the trend is almost the same at all the presented depths, indicating that the decline in drag to be due to the reduction in frontal area. It is also seen that the lowest drag values are either at the tank centre or free surface. At certain depth ratios such as 0.05 and 0.1, the drag generated at Cauchy numbers less than 2.6 is higher than 1, illustrating that the drag at these depths to be higher than equivalent rigid plate at tank centre. Post C_Y of 2.6, the reconfiguration numbers are less than 1 and begin to overlap for most of the depths, indicating that submergence depth does not a play a significant role after a certain Cauchy number.

Since this work involves studying the effect of submergence depth on drag generation, it is more prudent to define the reconfiguration number as the ratio of the drag experienced by the foil to that experienced by the equivalent rigid plate ($\Re^* = \frac{\overline{F}_d}{\overline{F}_{R_d}}$), when operating at the

same submergence depth. This method ensures that the comparision of forces is always occurring with respect to rigid plate at the same depth. Figure 4.7b presents this behavior and it can be immediately observed that this method results in presentation of the drag values of the rigid plate at 1 and the rest of the foils being lesser than 1, irrespective of the depth. Thus, it is explicit from this plot that the drag generated by the rigid plate to be the highest and that flexibility results only in drag reduction. Even in terms of comparision of the results with that from literature (Gosselin et al. (2010); Leclercq and de Langre (2016)), it can be observed that the $\Re^* - C_Y$ presents the results in better light, with $\Re^*$ values at most of the depths to be almost the same as that obtained by other researchers and that submergence depth does not have significance after a critical Cauchy number, which was also observed in figure 4.4.

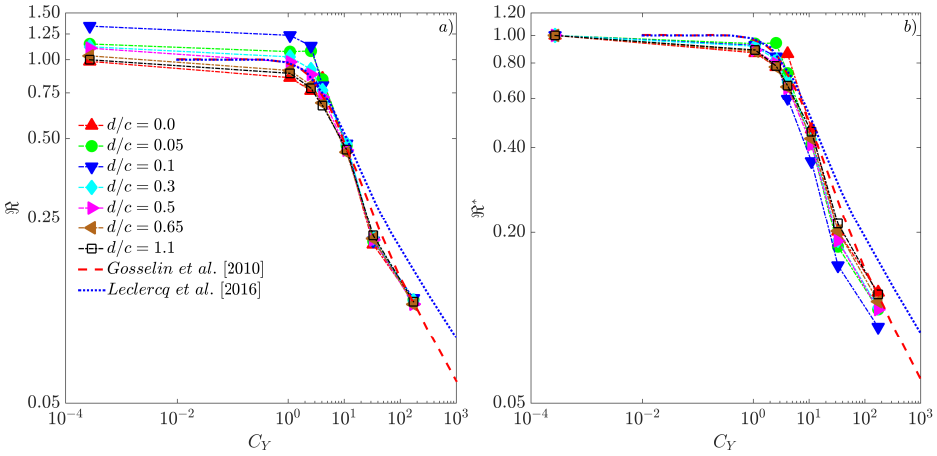

Figure 4.7: Variation of $\Re$ and $\Re^*$ with C_Y at specific depth ratios

Having presented the effect of reconfiguration in the previous section,

the Vogel exponents are calculated from the logarithmic slopes of the $\Re^* - C_Y$ plot at all the depths, that is $\Upsilon = 2\frac{\partial \ln \Re^*}{\partial \ln C_Y}$, where Υ is the Vogel exponent. So, a Vogel exponent of 0 signifies that the classical quadratic relationship of drag with velocity holds true while a value of -1 signifies a linear relation. Figure 4.8a presents the variation of the Vogel exponent with Cauchy number only at particular depths for the sake of clarity. It can be seen that the Υ is close to zero up to a Cauchy number of 1 for all of the depths presented, post which the exponent begins to decrease with an increase in C_Y. Barring a few points at C_Y of 4.1, it is observed that the lowest magnitude of the exponent occurs at C_Y of 11 for most of the depths, ranging from around -1.1 at the tank centre to -1.4 at the free surface. Further increase in Cauchy number results in an increase in the exponent value. Overall, this indicates that the quadratic relationship between drag and velocity does not hold true post a certain Cauchy number, irrespective of the depth and there exist certain Cauchy numbers where submergence depth has a strong influence on the drag-velocity scaling, but not on the rest.

In fact, this trend becomes explicitly clear when the Vogel exponents are plotted against submergence depth for different foils. Figure 4.8b presents this behavior, with the line markers and colours being the same as in Figure 4.4. It can be noticed that the trend of the exponent for the most rigid cases, that is of the rigid plate and C_Y of 1 are almost flat and close to zero. Increasing the Cauchy number brings a significant variation in the Υ magnitudes. At C_Y of 2.6 and 4, the

behavior is highly non-linear, with the lowest values being achieved at d/c of 0.1. At C_Y of 4.1, the exponent value at the free surface is almost equal to that at the tank centre- $\approx$ -0.7, distinct from that at C_Y of 2.6, where the exponent is far higher at the free surface than at the tank centre. At Cauchy number of 11, no such non-linear behavior is observed, rather the magnitude of the exponent increases monotonically from free surface to the tank center. On further increasing the C_Y values to 33 and 173, no such variations with respect to the depth are also observable and maintain almost a constant value of around -1 and -0.65, respectively.

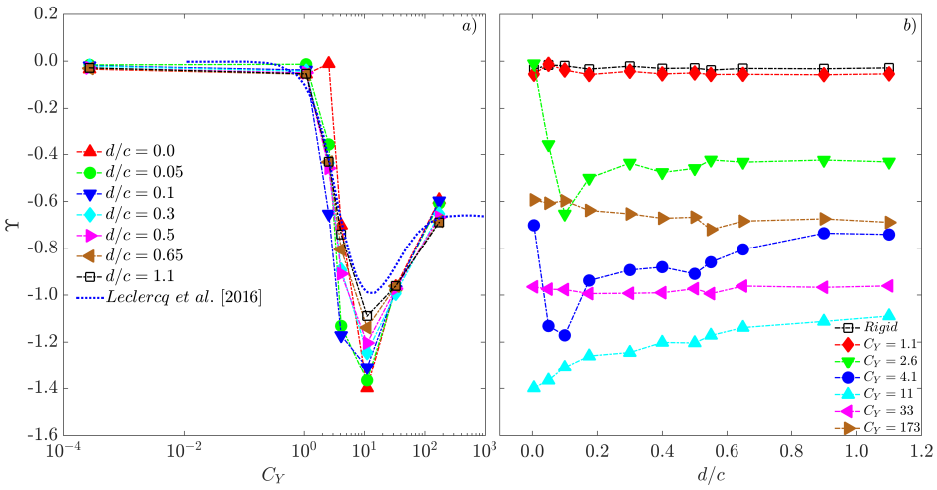

Figure 4.8: Variation of the Vogel exponent with Cauchy numbers and submergence depths

Leclercq and de Langre (2016) have calculated the Vogel exponents numerically with various flow profiles and their results in an uniform flow has been incorporated in figure 4.8a for comparision. It can be seen that the present results match favourably to their calcula-

tions, both in terms of the trend as well as magnitudes. Alben et al. (2004) and Gosselin et al. (2010) have shown through modelling of fibres and dimensional analysis for rectangular plates, respectively for cases involving large deformations that the Vogel exponent reaches an asymptotic value of -2/3 at high Cauchy numbers, which is close to the values obtained by us for C_Y of 173 when operating close to the tank centre. This indicates that the asymptotic limit has been reached, with further increase in C_Y expected to lead to marginal or even no changes in the magnitude of the Vogel exponent. In fact, Gosselin et al. (2010) and Leclercq and de Langre (2016) have stated that a near linear drag-velocity scaling is achieved theoretically and numerically at $C_Y = 10^{1.1} \approx 12.6$ due to the additive effects of area reduction and streamlining, which is close to experimental value of 11, at the tank centre.

4.3.5 Wake characterization

In this section, the results obtained by means of PIV show the evolution of the near wake region of the model. In figure 4.9, the flow fields resulting from PIV interrogations undertaken at 4 specific depths and with the foils with C_Y of 0.0003, 1, 4.1, 11, 33, and 173 are depicted, the flow being from left to right. Each row corresponds to models of different Cauchy numbers, while the submergence depth increases horizontally- starting from the free surface in the first column and ending with the tank centre. The submergence depths utilized for

the visualization in the current set of experiments (d/c = 0, 0.1, 0.4, and 1.1) have been selected based on the results obtained for the rigid plate. The colour map indicates the sign of the vorticity field with red for clockwise and blue for counter-clockwise directions. The thick black line indicates the location and the orientation of the models with flow, while the thick blue lines are used to indicate the approximate location of the free surface The free surface distortion was estimated from the PIV images using an in-house image processing code, with the distortions being visible only at low submergence depths and for models of low C_Y. The location of the sting has not been included here for the sake of clarity, but as described in the experimental set-up, was connected at the centre of all the investigated models. The PIV data being presented here is also averaged over a timespan similar to that presented in the previous chapter and corresponds to the steady part of the run which has been utilized for drag calculations, and the vorticity has been non-dimensionalized using the towing speed and chord.

A detailed explanation for the effect of the free surface on the rigid plates of AR = 0.25 and 0.5 appears in section 3.3.5. In the case of AR = 0.625 and the plate being rigid (plots 4.9a-4.9d), similar behavior is shown at the specified depths- a symmetric evolution of the time averaged vortices in the form of an elongated shear layer from the upper and lower edges whose symmetry breaks up with the reduction in submergence depth. This results in the interaction of gap-flow (d/c = 0.1) with free surface and formation of a strong

4.3 Results

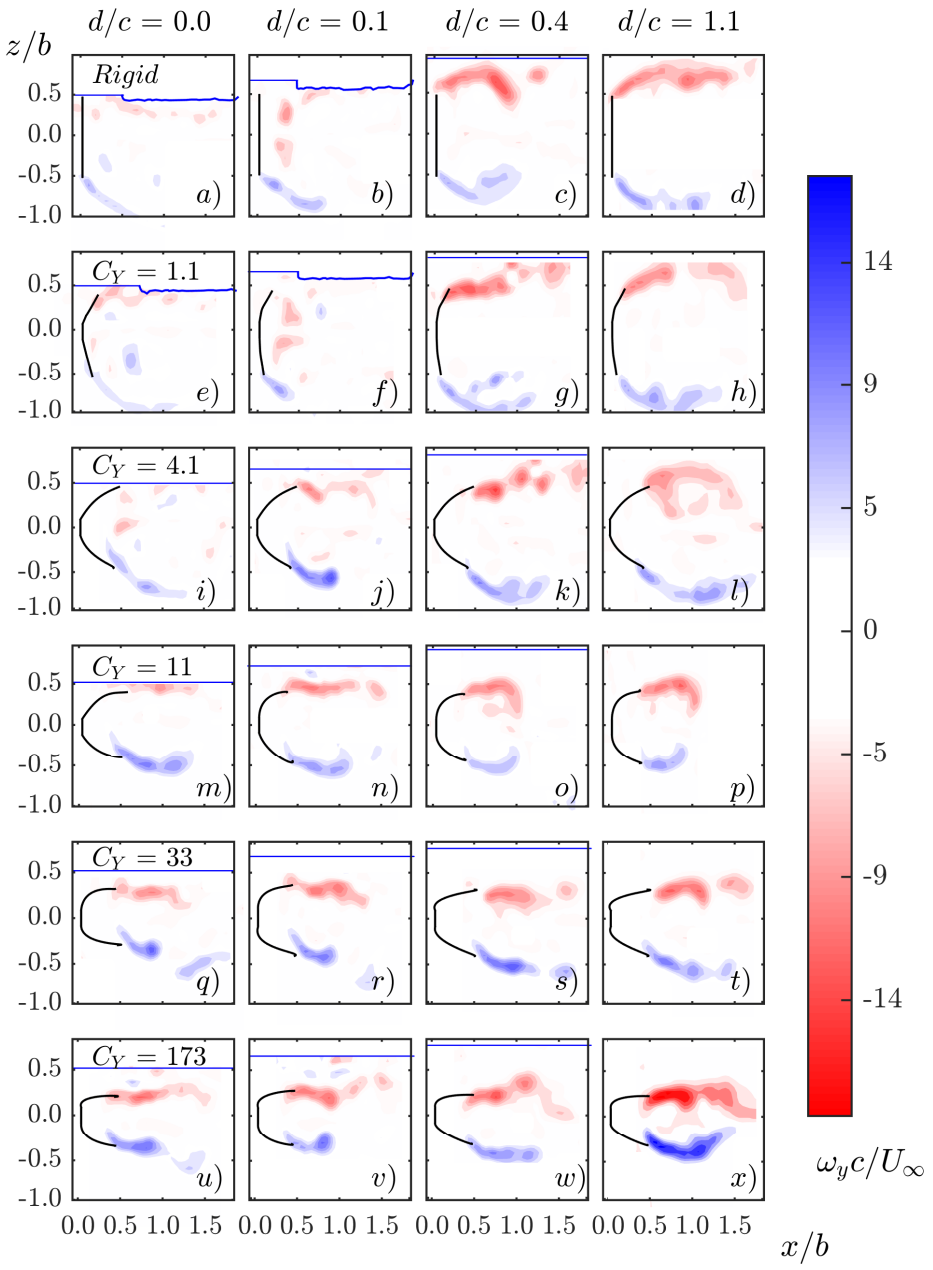

Figure 4.9: Near wake details for models of different C_Y and at specific depths, at Re_c of $6{\cdot}10^4$

asymmetric (with respect to span) recirculating flow enveloping the base region of the plate to a no flow condition over the upper edge and an elongated form near the lower edge at the free surface. For C_Y of 1.1 (plots 4.9e-4.9h), the aforementioned trends of the rigid plate seem to be replicated with a small weakening of the vorticities even though the foil does undergo a small deflection. This indicates the reason for the drag-depth plot to be similar to that presented by the rigid plate. At C_Y of 4.1, (plots 4.9i-4.9l), the foil deflections increase, resulting in further change in the near wake vorticities. The major difference when compared to previous cases is the absence of strong recirculating flow in the base region at d/c of 0.1 (plot 4.9j) while the weak, recirculating flow is still visible in plot 4.9i. This indicates that an increase in foil deflection results in an increase in effective submergence depth. This is the reason for shift in the location of the stronger base region recirculating flow from d/c of 0.1 to 0. Further increase in C_Y to 11 (plots 4.9m-4.9p) leads to greater foil deflection whose trajectory is almost the same at all the tested depths, thus exhibiting similar near wake profiles. The aspect of similar wake profile holds true even at Cauchy number of 33 and 173 (plots 4.9q-4.9x), apart from slight stretching of the wakes further downstream besides greater foil deflection at all the depths tested.

4.4 Discussion and Remarks

Although chapter 3 presented the trends of rigid plates near the free surface, the force and vorticity plots presented in the previous sections have provided an unique range of results for flexible systems. When the Cauchy number is increased to 1, the same phenomena is present at all the depths even though the model undergoes a small deflection due to fluid loading. This is observed in both force as well as PIV results. This indicates that the reconfiguration of the foil does reduce the drag generated but is not strong enough to alter the flow. Although no visualization tests have been done for the case of $C_Y = 2.6$, the variation of drag with depth mimics that of the previous 2 cases, indicating that the reduction of the frontal area is not significant enough to alter the near wake. Further increase in Cauchy numbers only intensifies the reconfiguration process, causing significant drag reduction. In fact, the abrupt drop in drag when submergence depth is reduced from d/c of 0.1 to 0 at low Cauchy numbers is missing in this situation, and the highest drag is observed at the free surface. This indicates that the fluid loading is strong enough to reconfigure the foil, resulting in the effective submergence depth to be greater than that established initially. So, when the foil is placed at free surface at the start of the experiment, it undergoes a reconfiguration process causing the effective submergence depth to be greater than 0, and the situation to be closer to d/c of 0.1 of the rigid case. The flow in the gap between the deflected upper edge and

free surface forms a recirculating zone in the near wake that envelops the base region, as visualized in figure 4.9i. Increasing the Cauchy number only enhances the area reduction process and consequently reduces drag, and the drag reduction being depth independent, as seen for $C_Y \geqslant 11$. In terms of the reconfiguration number, the trends presented here at all the depths match very well to that by Gosselin et al. (2010) and Leclercq and de Langre (2016), confirming that a C_Y greater than 1 always ensures drag reduction. Alben et al. (2002) presented in his analysis of the existence of a 'universal' deflection profile for the fibres and found a profile that was almost parabolic, while Gosselin et al. (2010) presented a model which indicated that at very high values of C_Y, the foil deflection ought to be such that its trailing edges are parallel to the flow but were not able to achieve the same experimentally due to flutter. In the current experiments, the comparision of classical beam theory solutions with the experimental positions indicated experimental deflection at C_Y of 173 to be lower (figure 4.5a), suggesting that there indeed exists a limit for the foil deflection.

In terms of the Vogel exponent, there is a transition of the drag velocity scaling from quadratic to linear and its variation with submergence depth. At very low C_Y, the exponents are almost 0 at all the submergence depths, indicating that the classical relationship holds true. As soon as C_Y increases to 2.6, a strong variation with submergence depth is observed, varying from 0 to around -0.4, suggesting that the drag-velocity scaling is sensitive to submergence

depth. Further increase in C_Y to 4.1 confirms this matter, but the band of values of Υ reduces, suggesting the scaling to be almost linear at low submergence depths ($d/c = 0.05, 0.1$). It is when the C_Y is 11 that the best performance in terms of Υ is displayed. At minimum, the drag-velocity scaling is linear and this occurs at the tank centre. The reduction in submergence depth in fact makes the behavior sub-linear, suggesting that the drag varies much more slowly when the foil is located closer to the free surface. PIV results also reveal the near wake vorticities to be altered, with the elongated wake profiles to be near parallel to the flow due to area reduction and streamlining effect. Also, the interaction of upper shear layer with free surface is such that the weakening of the wake occurs, with no recirculating bubble in the base region. At C_Y of 33, the fluid loading ensures greater area reduction and streamlining which causes lower drag, but the free surface has no significant effect on Vogel exponent. The loading ensures that the deflection results in a near parallel wake, and is always far from the influence of free surface, resulting in a near constant Υ. At C_Y of 173, Υ increases and reaches close to the asymptotic value of -2/3, as predicted by other researchers (Alben et al. (2004); Gosselin et al. (2010); Leclercq and de Langre (2016)).

Overall, in terms of drag generated, flexibility is always advantageous for drag reduction, with higher Cauchy numbers signifying greater area reduction and streamlining, and the drag reduction being significant at all depths.

Chapter 5

Strategic porosity

5.1 Overview

This chapter presents the methodology of data processing as well as the results of the analyses for rigid plates incorporating holes at strategic locations, with the focus of the study being the effect of holes, its orientation, and submergence depth on the drag generated.

5.2 Experimental Setup

All the experiments were conducted for a plate AR of 0.625 and Re_c of $6{\cdot}10^4$. These conditions were selected based on the trends observed in the earlier experiments (figure 3.3) wherein this particular plate presented a wide range of C_D values over the entire gamut of submergence depths tested, thereby acting as an ideal baseline model. The current experiments focused on studying the effect on a rectangular flat plate with the hole centers being located 14 mm from the upper and lower edges of the plate, respectively. This ensured that small variations in hole diameter will result in an insignificant change in the distance between the hole jet and the proximal plate

edge, with all the hole axes being parallel to the flow. In order to obtain holes at angles, the hole exit planes were maintained at the same distance from the plate edges while the hole inlet plane locations were varied, resulting in the jet angles (α) of either +45° or -45°, with the positive jet angle indicating the jet direction to be away from the model centerline in the downstream side of the plate. The hole diameter (h) and the number of holes (n_h) were varied such that the maximum porosity was always less than 10%. The constraint of the distance from the plate edge and the porosity were selected to ensure sufficient wall thickness existed between the holes and the corresponding proximal edges, and on the requirement of minimal change in the structural rigidity of model. The lateral spacing ratio of the holes, that is the ratio of hole center to center distance to the hole diameter was also fixed at 1.1. Table 5.1 presents characteristics of the fabricated models and figure 5.1 a schematic of the model.

Table 5.1: Characteristics of the porous models

Case	h $\cdot 10^{-3}$ **m**	n_h	$\boldsymbol{\beta}$ **%**	α (°)
1	10	30	9.4	0
2	7	42	6.5	0
3	10	30	9.4	-45
4	10	30	9.4	+45

The models were mounted as described in section 3.2, at various positions ranging from a depth such that the upper edge of the plate was located at the free surface, to a depth at which the upper and lower

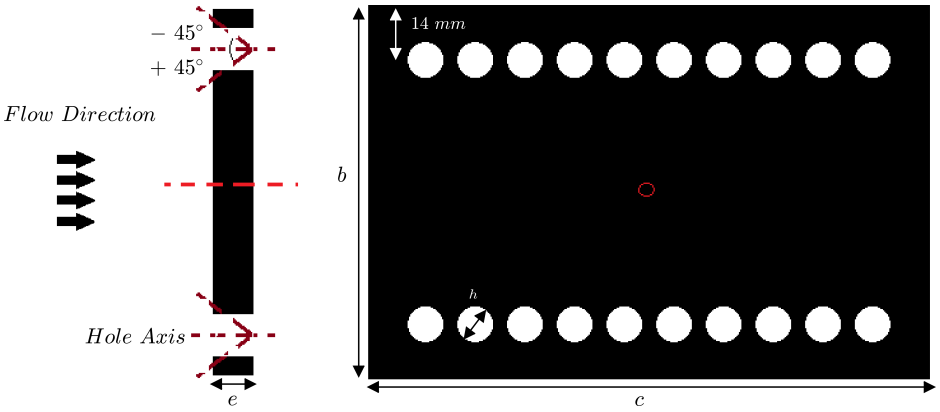

Figure 5.1: Schematic of the plate with holes

plate edges were equidistant from the free surface and the ground. The submergence depth was always measured as the distance between the upper edge of the plate and free surface. Each run was repeated five times to ensure repeatability of the results. The mean plate drag force ($\overline{F}$) was non-dimensionalized using the expression,

$$C_D = \frac{\overline{F}}{\frac{1}{2}\rho U_\infty^2 A^*} \tag{5.1}$$

where A^* corresponds to the actual exposed area, accounting for the reduction in area due to the holes.

5.3 Results

Similar to the cases with the rigid plate as described in chapter 3, the force signals exhibit 2 prominent force peaks and were disregarded for

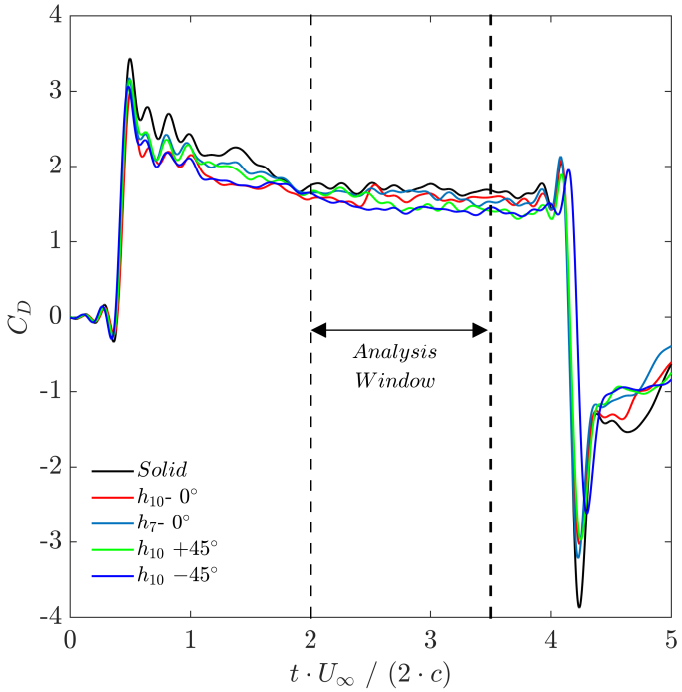

Figure 5.2: Non-dimensional force signal against non-dimensional time for all the models at tank centre.

steady force calculations. Thus, the time windows were selected on a similar basis, along with an offset of 0.5 s from the end-point were selected for drag coefficient calculations. Figure 5.2 presents a typical non-dimensional force signal resulting from one of the experiments for each of the models at Re_c of $6{\cdot}10^4$, at the tank centre against non-dimensional time.

5.3.1 Effect of holes on drag forces with submergence depth

In this section, the effect of porosity on drag is studied for all models with the hole axes being parallel to the towing direction ($\alpha = 0°$), at different submergence depths. The submergence depth has been non-dimensionalized using the chord, with 0 corresponding to free surface and 1.1 to the tank centre.

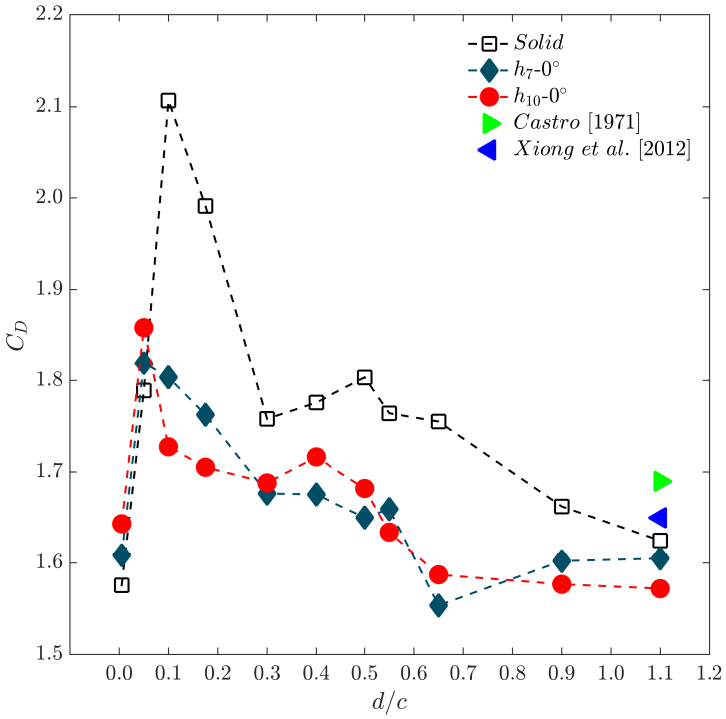

Figure 5.3: Variation of C_D with depth ratio at different hole diameters for cases with hole axes parallel to the flow.

Figure 5.3 presents the variation of drag with depth, with □ representing the solid plate and ♦, ● the models with holes of 7 and 10

mm diameters, respectively. It can be seen that the trends exhibited by the porous models are similar to that of the solid case but with the magnitudes of drag coefficient being lower. There is a monotonic increase in drag as the submergence depth is reduced from the tank centre value, with a region displaying a change in the gradient when $0.2 \leqslant d/c \leqslant 0.5$, leading to an abrupt rise in drag at d/c of 0.05 and finally reducing at free surface. Although the model with 7 mm holes also exhibits this behavior, neither the decrease in drag coefficient at the tank centre nor at d/c of 0.1 are significant as that compared to the model with holes of 10 mm diameter. Note that the C_D values for the porous models have been calculated using the actual exposed area, that is an area less than that of the rigid plate on account of the holes. This reduction in drag occurs at all submergence depths, the reduction with respect to the rigid plate being on the order of 3% at the tank centre and around 18% at d/c of 0.1, and the drag peak location of the porous models being shifted closer to the free surface. In fact, the results at tank centre compare favourably to experimental and computational results of Castro (1971) and Xiong et al. (2012), respectively. The experiments by Castro (1971) were accomplished on two dimensional plates over a wide range of porosities and with Re ranging $2.5{\cdot}10^4$ to $9{\cdot}10^4$. The difference in drag between the current results and that obtained by Castro (1971) for plates with porosity of 10% is less than 10%, indicating that the method as well as the analysis procedure holds good even for cases of low porosity. The drag values at free surface are slightly higher than that of the rigid

case, indicating their effect in terms of drag reduction at the free surface to be minimal. Overall, this indicates that holes located near the edges have a strong effect on the drag generated. This was previously observed by Huera-Huarte (2014) in experiments with circular plates in cross-flow used to model sport equipment. The author linked the drag reduction provided by the holes to the modification of the shear layer detachment in the plate. The coaxial jets formed in the holes near the edges moved the shear layer interaction region further away from the plate, thus lowering the overall C_D. The results obtained in figure 5.3 indicate that a similar phenomena occurs in rectangular plates with holes close to the edges and located at tank centre. Flow visualization results are presented in the subsequent section to identify the source of drag reduction in the porous model compared to the solid plate, at low submergences.

5.3.2 Effect of hole inclination on drag forces with submergence depth

Since a significant reduction in drag was observed in the model with holes of 10 mm diameter, the effect of tilting the hole axis with respect to the flow direction was also investigated and is presented in this section. As explained earlier, the jet angles have been obtained by maintaining the hole exit plane locations at the same distance from the plate edges while the hole inlet planes have been relocated based on the requisite angle.

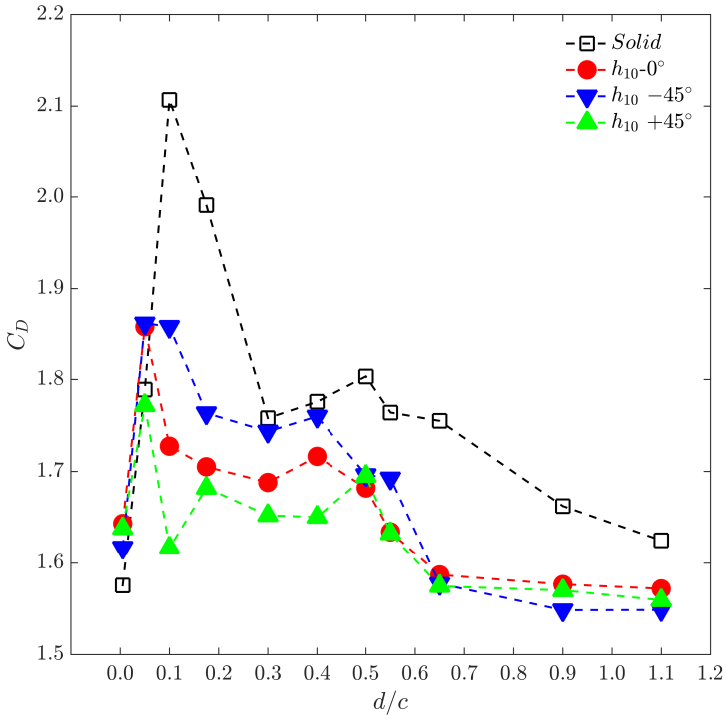

Figure 5.4: Variation of drag coefficient with depth ratio for different hole angles.

The trends for the solid plate as well as porous $\alpha = 0°$ case have also been plotted for the sake of comparision in figure 5.4, while ▲, ▼ represent the jet angles of 45° oriented away and towards the model centerline, respectively. The data shows clearly how an inclination in the hole axis with respect to the flow direction has a strong effect on the drag generated. The trends of the models involving inclined holes follow that of holes parallel to the flow but with drag magnitudes being lower or higher, dependent on the hole inclination. For all the cases involving the holes, the drag values at the tank centre and the free surface are similar, suggesting mild efficacy when the free

surface is far from the plate. When the holes are tilted towards the centerline, the drag values are lower than the solid model but higher than $\alpha = 0°$ case. A significant reduction in drag is observed over the entire range of submergence depths when the holes are tilted away from the centerline, with the reduction being most prominent at d/c of 0.1. Perera (1981) studied the orientation of porosity, in the form of horizontal or vertical slots spanning the entire length in fence models and found that the level of porosity has a stronger influence on the wake rather than its orientation. However, the current results show that the aspect of directionality as well as its proximity not only to the plate edge but also the free surface has a strong effect on the total drag. The results from flow visualization are presented in the following section to understand the observed force trends.

5.3.3 Wake characterization

The PIV results have been presented in this section involving vorticities, with the plot specifications and the colormap being same as that in the previous chapters, similar to the last column of figures 3.7 and 3.8, due to the focus of the measurements being the steady flow scenario. However, the non-dimensionalization here is with respect to chord instead of hydraulic diameter. The visualization has been undertaken at specific depths based on the results observed for the solid plate and model incorporating holes of 10 mm diameter. Figure 5.5 presents results for the cases of solid plate and the plate with

holes parallel to the flow at Re_c of $6{\cdot}10^4$ and d/c of 0.1 and 1.1. These depths have been selected based on the results observed in chapter 3 for AR of 0.625, with these depths corresponding to the location of the drag peak and the tank centre, respectively, as seen in figure 4.9. The green lines in the plots of porous models indicate the approximate location and orientation of the holes for reference and comparision.

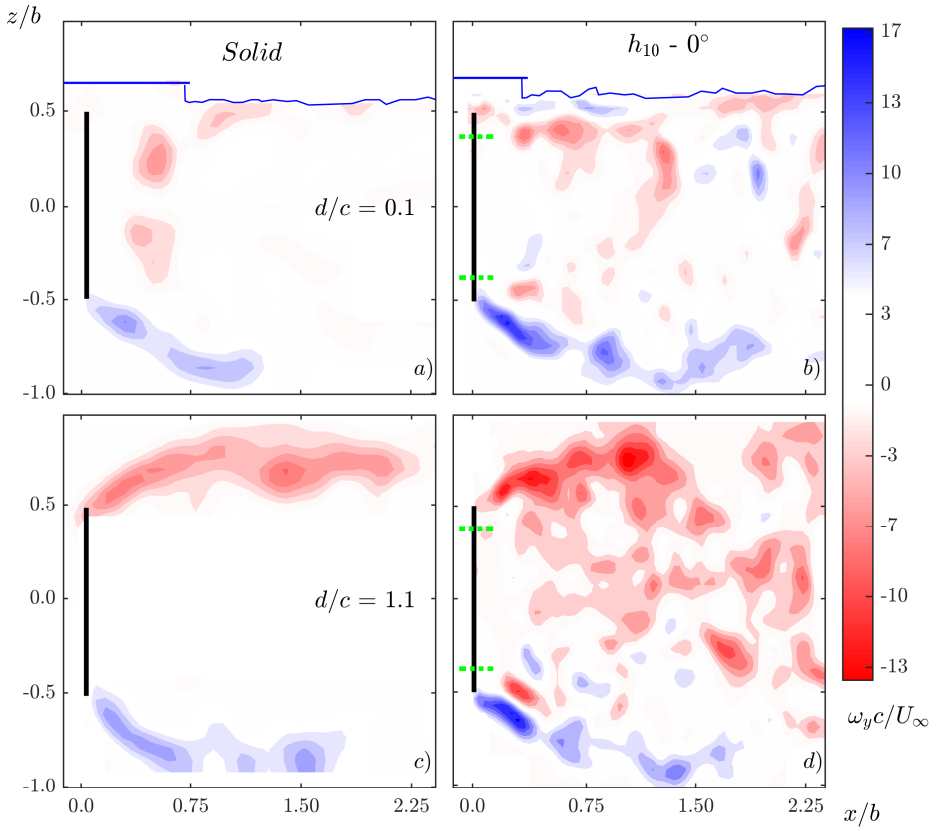

Figure 5.5: Wake features for solid plate (first column) and a porous model ($\alpha = 0°$) at $d/c = 0.1$ and tank centre

For the solid plate case at tank centre (plot 5.5c), the symmetric

evolution of elongated shear layers and at $d/c = 0.1$ (plot 5.5a), the asymmetric wake due to the interaction of the gap-flow with the free surface and a strong recirculating flow in the base region are similar to that observed in the previous chapter (plots 4.9d, 4.9b). Plot 5.5d presents wake features of porous model at tank centre and is similar to that exhibited by the solid plate, barring for the presence of a pair of vortices near the hole location and close to the lower plate edge. The orientation of these vortices is skewed towards the shear layer, as has also been reported by Theunissen and Worboys (2018) in their work involving holes on circular plates. This indicates that the skewing of the jets towards the shear layer is not dependent on the model geometry but on the proximity of the holes to the plate edges, as previously described by Huera-Huarte (2014). The most significant difference in the wake is visible in plot 5.5b wherein the recirculating flow existing in the plate wake is located at a greater downstream distance ($x/b \sim$1.1) than that observed for the solid plate ($x/b \sim$0.5). For the solid plate at low submergence, the interaction of the gap-flow with the plate shear layer and free surface has been identified as the source of drag peak, as presented in chapter 3. This indicates that the jets emanating from the upper holes interact with the gap-flow, shear layer and the free surface, resulting in a greater downstream excursion of the recirculation zone.

The effect of hole angle is discussed in figure 5.6. The first column corresponds to the condition of hole axis being parallel to the flow ($\alpha = 0°$), the second column to the case with hole axis towards the

model centerline ($\alpha = -45°$) and the last in the opposite direction ($\alpha = +45°$). The submergence depths shown in the figure have been selected after the phenomena described in the force plot of figure 5.4.

At the tank centre (plots 5.6m-5.6o), the symmetric layout of the shear layers is visible in all the hole configurations, and no major observable differences in the wake seems to be introduced by the hole angle. As the submergence depth is reduced (plots 5.6j-5.6l), the free surface has an effect on the proximal plate edge shear layers and the hole jets, resulting in its evolution to be near parallel to the free surface. This is very different from the case of the solid plate which has been presented in the preceding chapter (plots 4.9a-4.9d). At d/c of 0.1, which corresponds to the location of drag peak for the solid plate, it is clearly visible in all the hole configurations (plots 5.6g-5.6i) that the presence of jets results in an asymmetric recirculating flow due to the interaction of the gap-flow and free surface to occur further downstream when compared to the solid plate. The location of the recirculating flow is also seen to be dependent on the hole orientation, with the location being the farthest in the case of plate with holes tilted outward from the model centerline ($x/b \approx 1.5$) and $x/b \approx 1.1$ in the other 2 porous models. At the location of drag peak for all the hole configurations, that is d/c of 0.05, it is seen (plots 5.6d-5.6f) that the free surface gap-flow interaction is stronger than the effect of the hole jet, resulting in the formation of a recirculating flow in the base region of the plate, with the location being dependent on the hole angle. The recirculating region is observed to be located

closer to the model ($x/b < 0.75$) when the jets are angled towards the centerline than when away from it ($x/b \approx 0.75$). At free surface, the wakes of the 3 configurations (plots 5.6a-5.6c) are similar, indicating the same or limited effect of the hole orientation.

The magnitude of the velocities ($U = \sqrt{u^2 + w^2}$), non-dimensionalized with the towing velocity are plotted for the porous models in figure 5.7 at the same depths as those in figure 5.6. The colormap indicates red to be the highest velocity and blue the lowest, with black dotted lines indicating the orientation and location of the holes. The velocity fields again emphasize the observations made based on vorticities. The symmetric evolution of the shear layers at the tank centre for all the model configurations (plots 5.7m- 5.7o) indicates that the orientation of the holes has no significant effect, besides a slight reduction or extension of the wake region downstream the plate when the holes are towards or away from the centerline, respectively. The break in the symmetry is observed as the submergence depth is reduced (plots 5.7j- 5.7l), with a region of significant flow velocity in the base region of the plate, whose size is clearly dependent on the hole orientation. At d/c of 0.1 (plots 5.7g- 5.7i), the interaction of the hole jet with the gap-flow is clearly visible and results in a greater downstream excursion of wake, as explained in figure 5.5. Further reduction in submergence depth to d/c of 0.05 results in an observable variation in the wake velocities (plots 5.7d- 5.7f), which is dependent on the hole orientation. When the holes are tilted away from the model centerline, the high velocity region of the wake is observed at $x/b \approx 0.75$

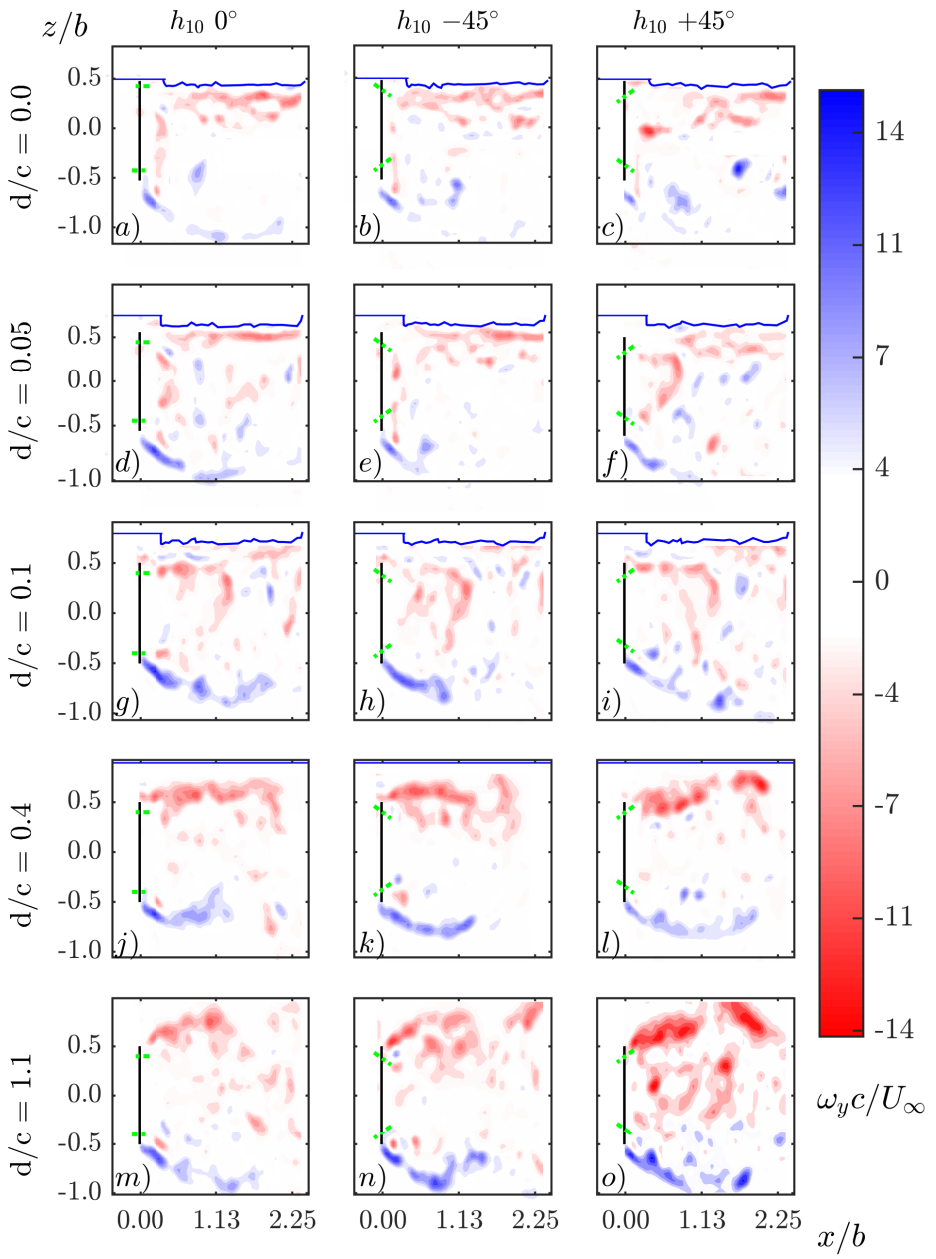

Figure 5.6: Wake characteristics for different hole angles at specific depths, at Re_c of $6{\cdot}10^4$

which reduces to $x/b \approx 0.5$ when the holes are parallel to the flow and shrinks further when the holes are tilted towards the model centerline. At free surface (plots 5.7a-5.7c), the wake velocities are similar in the three cases indicating limited impact of hole orientation, which was also observed in plots 5.6a-5.6c.

With the greatest reduction in drag being observed when the jets are inclined in a direction away from the model centerline, wake velocities and streamlines are plotted and compared against that observed for the solid plate, as seen in figure 5.8. At d/c of 1.1, (plots 5.8c-5.8d), the velocity distribution in the wake for the solid and porous model are similar, apart from the greater downstream location of the recirculating region in the porous case. At $d/c = 0.1$, the characteristics (plots 5.8a-5.8b) are starkly different. For the solid plate, the gap-flow free surface interaction results in the location of the high velocity region to be asymmetrically distributed about the span in the base region ($x/b \leqslant 0.75$), whereas in the porous model, the features associated with the gap-flow and free surface interaction is located further downstream ($x/b < 1.5$) than for the solid plate.

5.4 Discussion and Remarks

The force plots showed that the presence of holes result in drag reduction. Though the effect of porosity on cross-flow plates has been studied earlier by several researchers, the effect of locating them

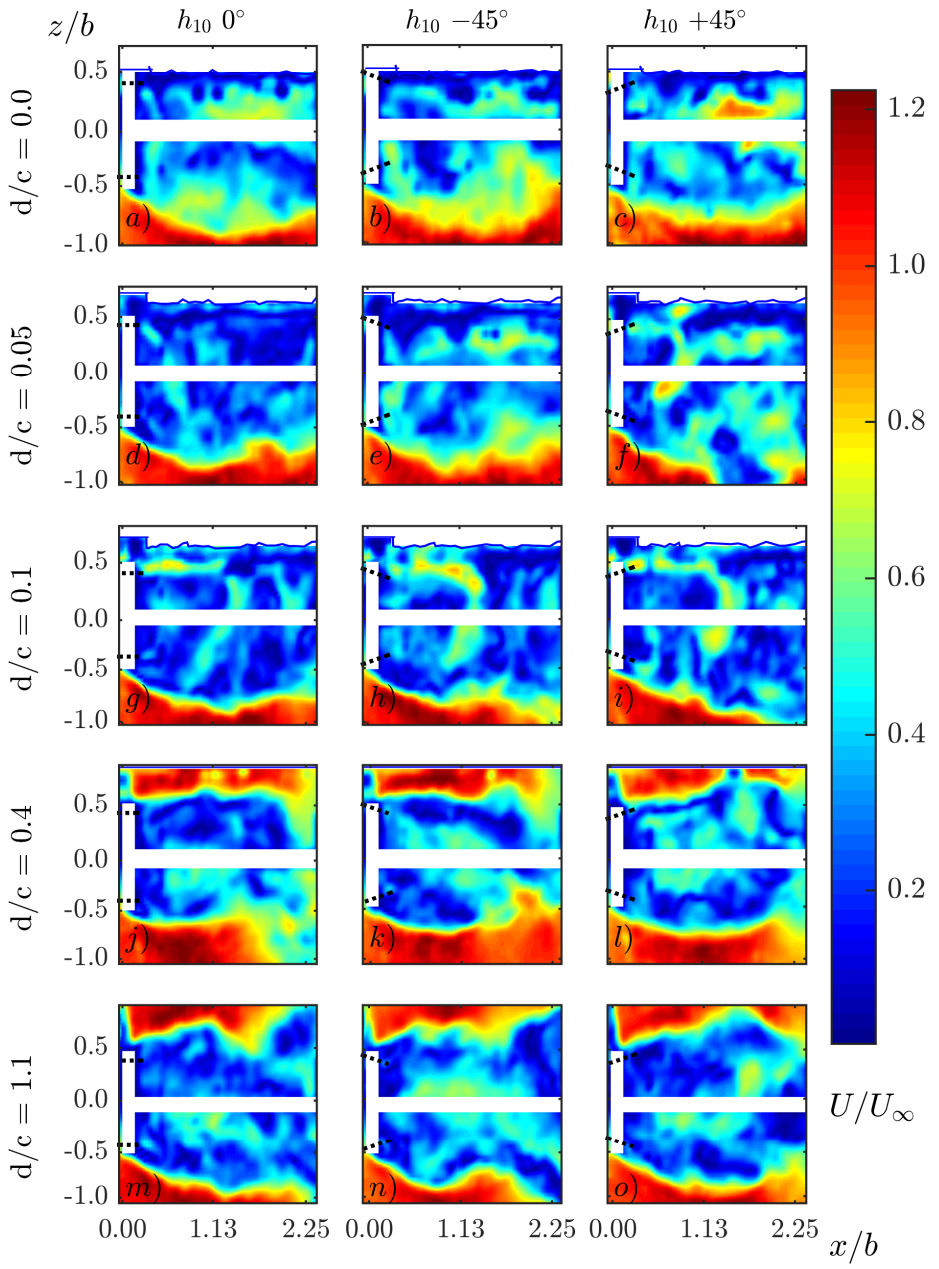

Figure 5.7: Porous model wake velocities at different hole angles and specific depths, with the white region denoting the model and shaft.

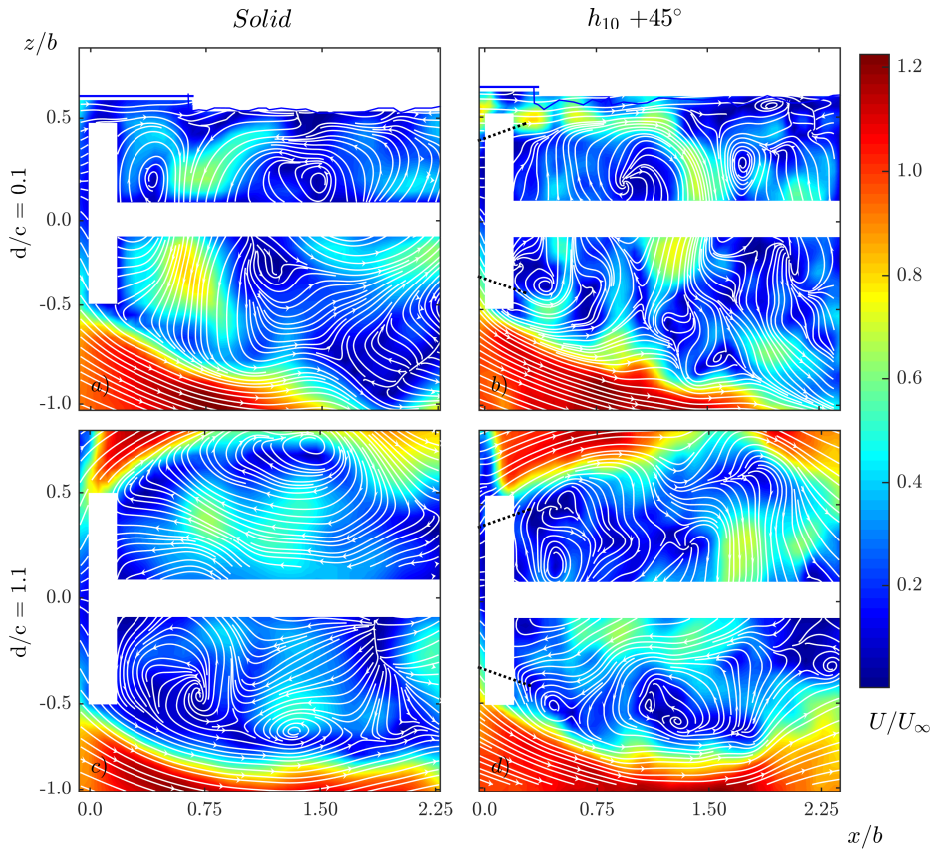

Figure 5.8: Wake velocity comparision for solid (first column) and porous model, with the white region denoting the model and shaft. ($\alpha = +45°$)

at particular locations and the effect of orientation for rectangular plates, when operating in proximity to the free surface has not been done. The results by Castro (1971) over a wide range of porosities on rectangular plates indicated a critical porosity value ($\beta \approx 15\%$) post which the drag reduction is extremely rapid. But, at low porosities, similar to that in the current scenario, the drag reduction was mild. The findings by Roberts (1980) for slotted circular disks indicated

that porosity as well as their arrangement played a significant effect on the drag generated. The present results for a rectangular plate with holes being distributed close to the plate edges also indicate a similar dependency. Huera-Huarte (2014) observed drag reduction, with respect to a solid circular plate of approximately 7% when the holes were located close to the periphery. The results at the tank centre for 10 mm parallel holes are close to these findings, the reduction being $\mathcal{O}(3\%)$. This can mainly be attributed to the difference in model geometry and the different hole distribution from the periphery. Overall, the drag reduction is due to the interaction of the hole jet with the shear layers generated from the plate edges, with larger C_D reduction being achieved when near the free surface. The magnitude as well as the location of the drag peak is altered due to the presence of the holes, as observed in figure 5.3. Moreover, it has been shown here that the orientation of the holes is important as well. By varying the angle of the hole jet, a major variation in drag values can be obtained. This is due to the change in the distance at which the hole jet interacts with the shear layer. The results indicate that the drag reduction is highest when the holes are oriented such that the plate shear layers are pushed away from the model centerline as seen in the wake plots, with this action being explicit at d/c of 0.05 and culminates in the recirculating flow to occur further downstream rather than in close proximity to base region of the plate. This results in a drag reduction with respect to the solid plate of $\sim 23\%$, compared to $\sim 18\%$ achieved with parallel holes.

Chapter 6

Summary and Future work

The work presented in this thesis focuses on understanding the mechanism of interaction of the free surface of a fluid with a canonical structure, a rectangular plate being towed cross-flow over a wide range of submergence depths and Reynolds numbers, and its effect on the horizontal force, to finally its modulation using two different approaches– strategically located holes and structural flexibility.

The rigid flat plate experiments act as a foundation for understanding the behavior of free surface on drag generation. When plates are away from the free surface, drag forces showed minimum values for aspect ratios close to 1. The trends were also found to be insensitive to changes in the Reynolds number investigated, except when $0.75 \leqslant AR \leqslant 1.33$. Conversely, the trends with changing submergence depth were observed to be clearly dependent on Reynolds number, and on aspect ratio to a smaller extent. These experiments indicated that the drag increased abruptly at low submergence depths for almost all of the plates, due to the interaction between the free surface, the resultant gap-flow and the upper shear layer. This interaction leads to the formation of a recirculating flow in close proximity to the base region of the plate, due to the ability of free surface to distort and

enable fluid entrainment. The value of the drag at this submergence is modulated by how much the gap-flow is deflected and how close it ends up being the recirculation region from the plate.

Having described the physics associated with the drag phenomena near the free surface, two different model configurations were studied. One is the concept of strategic porosity. Although the effect of porosity, and its spatial distribution in circular disks has been looked at in earlier studies and shown the benefit of drag reduction, its effects in rectangular plates and near the free surface has not been explored. These experiments have shown that the presence of holes leads to drag reduction at most of the depths, with its effect being greatest at low depths. Although there still exists a jump in drag values at low submergences, the magnitude is reduced significantly. The drag reduction occurs due to the interaction of the jets formed at the holes, the proximal plate shear layer and the gap flow which results in a larger area of recirculating flow. Besides the location of the holes, the angle of the hole jet with respect to the flow also affects the drag, with the greatest drag reduction being achieved when the holes were inclined such that the plate shear layers were pushed away from the model centerline.

Another method studied during the course of this thesis was structural flexibility. The study showed that structural flexibility is always an asset with regards to drag mitigation. In fact, it fared better than the previous concept with the drag peak observed in the rigid plate

being virtually non-existent, post a particular magnitude of flexural stiffness. There appears to be a critical Cauchy number C_{Y_1}, $4.1 \leqslant C_{Y_1} \leqslant 11$ over which the drag variation is depth independent rather than the behaviour exhibited at $C_Y \leqslant 2.6$. With respect to the Vogel exponents, the behavior at low flexibility is similar to that shown by classical systems at all depths that is, a quadratic scaling. However, there is a critical C_{Y_2}, $4.1 \leqslant C_{Y_2} \leqslant 33$ that implies the Vogel exponents to be lesser than -1 and independent of depth. Further increase in Cauchy number (> 173) is not expected to provide significant changes with respect to the scaling, and thus the behavior remain asymptotic. More experiments ought to be conducted in order to check if $C_{Y_1} \approx C_{Y_2}$ and the existence of a 'universal' deflection profile.

All through the thesis, the focus has been on understanding the effect of free surface on the horizontal force. Previous studies involving cylinders have shown existence of a vertical component of force at low submergences. With the observed flow asymmetry at low depths as well as certain similarities in Froude number studies involving the plates and cylinders, it is expected that vertical forces are bound to come into this scenario too. Whether their behaviour is similar to that observed in the cylinders or their variation amongst the aforementioned model configurations can be substantiated only with more experiments. Another aspect is wave drag. Though its effect is obviously included in total drag measurements, its individual contribution to the total has not been estimated.

Chapter 6 Summary and Future work

From a fluid dynamics standpoint, flexible structures show lower drag than strategic porosity. However this drag reduction comes at a price, the very same flexural stiffness values being low which may or may not be acceptable from an engineering point of view when the structure is also expected to be a part of a load bearing member, or due to its large displacements. Moreover, with the ability of the structure to deform generously under loading, the premise of the member being a bluff body also comes into question. This makes the method of utilizing holes highly promising for immediate and easy implementation in current systems. Moreover, by optimizing the size, location, orientation, and porosity, it is expected to perform far better than that presented in this work. As a matter of fact, more concepts involving strategic porosity are being pursued currently, and to identify their operational limits. For example, implementation of strategic porosity in the foundation structures of offshore wind turbines and oil rigs is expected to not only realize in lower hydrodynamic loads acting on them thus increasing their lifespan but also provide an opportunity to optimize the design as well. In general, both these techniques show great promise of drag mitigation near the free surface and a mixture of both these methods is expected to provide a balance between drag mitigation and structural rigidity.

Bibliography

S. Alben, M. Shelley, and J. Zhang. Drag reduction through self-similar bending of a flexible body. *Nature*, 420(6915):479, 2002.

S. Alben, M. Shelley, and J. Zhang. How flexibility induces streamlining in a two-dimensional flow. *Physics of Fluids*, 16(5):1694–1713, 2004.

T. Arslan, S. Malavasi, B. Pettersen, and H. I. Andersson. Turbulent Flow Around a Semi-Submerged Rectangular Cylinder. *Journal of Offshore Mechanics and Arctic Engineering*, 135(4):041801, 2013. ISSN 0892-7219.

A. Benusiglio, F. Chevy, É. Raphaël, and C. Clanet. Wave drag on a submerged sphere. *Physics of Fluids*, 27(7):072101, jul 2015.

B. Bouscasse, A. Colagrossi, S. Marrone, and A. Souto-Iglesias. SPH modelling of viscous flows past a circular cylinder interacting with a free surface. *Computers & Fluids*, 146:190–212, 2017. ISSN 00457930.

I. P. Castro. Wake characteristics of two-dimensional perforated plates normal to an air-stream. *Journal of Fluid Mechanics*, 46 (3):599–609, 1971.

BIBLIOGRAPHY

D. Chen and G. Jirka. Experimental study of plane turbulent wakes in a shallow water layer. *Fluid Dynamics Research*, 16(1):11, 1995.

I. Cho and M. Kim. Wave absorbing system using inclined perforated plates. *Journal of Fluid Mechanics*, 608, 2008.

I. G. Currie. *Fundamental mechanics of fluids*. CRC Press, 2012.

S. C. R. Dennis and A. Chadna. The steady channel flow of a viscous incompressible fluid past a normal, flat plate. *Research Report*, 1995.

S. C. R. Dennis, W. Qiang, M. Coutanceau, and J. L. Launay. Viscous flow normal to a flat plate at moderate Reynolds numbers. *Journal of Fluid Mechanics*, 248:605–635, 1993. ISSN 14697645.

ESDU. Fluid forces and moments on flat plates. *Engineering Science Data Unit 70015*, 1970.

A. Fage and F. C. Johansen. On the flow of air behind an inclined flat plate of infinite span. *Proceedings of the Royal Society of London, Series A*, 116(773):170–197, w 1927.

R. Fail, J. Lawford, and R. Eyre. Low-speed experiments on the wake characteristics of flat plates normal to an air stream. *ARC Technical Report 3120*, 1959.

J. N. Fernando and D. E. Rival. Reynolds-number scaling of vortex pinch-off on low-aspect-ratio propulsors. *Journal of Fluid Mechanics*, 799:R3, 2016a. ISSN 0022-1120.

J. N. Fernando and D. E. Rival. On vortex evolution in the wake of

axisymmetric and non-axisymmetric low-aspect-ratio accelerating plates. *Physics of Fluids*, 28(1):017102, 2016b. ISSN 10897666.

M. Ghisalberti and H. Nepf. Mixing layers and coherent structures in vegetated aquatic flows. *Journal of Geophysical Research: Oceans*, 107(C2), 2002.

F. P. Gosselin, E. de Langre, and B. A. Machado-Almeida. Drag reduction of flexible plates by reconfiguration. *Journal of Fluid Mechanics*, 650:319–341, 2010.

R. W. F. Gould. Wake blockage corrections in a closed wind tunnel for one or two wall-mounted models subject to separated flow. *ARC Technical Report 3649*, 1969.

D. L. Harder, O. Speck, C. L. Hurd, and T. Speck. Reconfiguration as a prerequisite for survival in highly unstable flow-dominated habitats. *Journal of Plant Growth Regulation*, 23(2):98–107, 2004.

A. Hemmati, D. H. Wood, and R. J. Martinuzzi. Effect of side-edge vortices and secondary induced flow on the wake of normal thin flat plates. *International Journal of Heat and Fluid Flow*, 61:197–212, 2016a.

A. Hemmati, D. H. Wood, and R. J. Martinuzzi. Characteristics of distinct flow regimes in the wake of an infinite span normal thin flat plate. *International Journal of Heat and Fluid Flow*, 62:423–436, 2016b.

P. Hémon. Hydrodynamic characteristics of sea kayak traditional paddles. *Sports Engineering*, 21(3):189–197, 2017.

BIBLIOGRAPHY

J. D. Hudson and S. C. R. Dennis. The flow of a viscous incompressible fluid past a normal flat plate at low and intermediate Reynolds numbers: the wake. *Journal of Fluid Mechanics*, 369(160), 1985.

F. J. Huera-Huarte. Some observations on the flow physics of paddle racquets. *Proceedings of the Institution of Mechanical Engineers, Part P: Journal of Sports Engineering and Technology*, 228(1):40–48, 2014.

H. Kim and S. Lee. Hole diameter effect on flow characteristics of wake behind porous fences having the same porosity. *Fluid Dynamics Research*, 28(6):449, 2001.

G. Kirchhoff. Zur theorie freier flüssigkeitsstrahlen. *Journal für die reine und angewandte Mathematik*, 70:289–298, 1869.

P. Koumoutsakos and D. Shiels. Simulations of the viscous flow normal to an impulsively started and uniformly accelerated flat plate. *Journal of Fluid Mechanics*, 328(1989):177–277, 1996. ISSN 0022-1120.

T. Leclercq and E. de Langre. Drag reduction by elastic reconfiguration of non-uniform beams in non-uniform flows. *Journal of Fluids and Structures*, 60:114–129, 2016.

D. Lisoski. *Nominally two dimensional flow about a normal flat plate*. PhD thesis, California Institute of Technology, 1993.

I. H. Liu, J. Riglin, W. C. Schleicher, and A. Oztekin. Flow past a plate in the vicinity of a free surface. *Ocean Engineering*, 111: 323–334, 2016. ISSN 00298018.

BIBLIOGRAPHY

M. Luhar and H. M. Nepf. Flow-induced reconfiguration of buoyant and flexible aquatic vegetation. *Limnology and Oceanography*, 56 (6):2003–2017, 2011.

S. Malavasi and A. Guadagnini. Interactions between a rectangular cylinder and a free-surface flow. *Journal of Fluids and Structures*, 23(8):1137–1148, 2007. ISSN 08899746.

S. Malavasi, G. Messa, U. Fratino, and A. Pagano. On the pressure losses through perforated plates. *Flow measurement and instrumentation*, 28:57–66, 2012.

H. Miyata, N. Shikazono, and M. Kanai. Forces on a circular cylinder advancing steadily beneath the free-surface. *Ocean Engineering*, 17 (1-2):81–104, 1990. ISSN 00298018.

F. M. Najjar and S. Balachandar. Low-frequency unsteadiness in the wake of a normal flat plate. *Journal of Fluid Mechanics*, 370(1998): 101–147, 1998. ISSN 00221120.

F. M. Najjar and S. P. Vanka. Effects of intrinsic three dimensionality on the drag characteristics of a normal flat plate. *Physics of fluids*, 7:2516–2518., 1995a.

F. M. Najjar and S. P. Vanka. Simulations of the unsteady separated flow past a normal flat plate. *International Journal for Numerical Methods in Fluids*, 21(7):525–547, 1995b. ISSN 10970363.

V. D. Narasimhamurthy and H. I. Andersson. Numerical simulation of the turbulent wake behind a normal flat plate. *International*

Journal of Heat and Fluid Flow, 30(6):1037–1043, 2009. ISSN 0142727X.

K. J. Niklas. Petiole mechanics, light interception by lamina, and economy in design. *Oecologia*, 90(4):518–526, 1992.

X. Ortiz, D. Rival, and D. Wood. Forces and moments on flat plates of small aspect ratio with application to PV wind loads and small wind turbine blades. *Energies*, 8(4):2438–2453, 2015.

M. D. A. E. S. Perera. Shelter behind two-dimensional solid and porous fences. *Journal of Wind Engineering and Industrial Aerodynamics*, 8(1-2):93–104, 1981.

M. Reichl, P., Hourigan, K., Thompson. Flow past a cylinder close to a free surface. *Journal of Fluid Mechanics*, 533:269–296, 2005.

M. J. Ringuette, M. Milano, and M. Gharib. Role of the tip vortex in the force generation of low-aspect-ratio normal flat plates. *Journal of Fluid Mechanics*, 581:453, 2007. ISSN 0022-1120.

B. Roberts. Drag and pressure distribution on a family of porous, slotted disks. *Journal of Aircraft*, 17(6):393–401, 1980.

A. Roshko. On the drag and shedding frequency of two-dimensional bluff bodies. *NACA Technical Report 3169*, 1954.

J. Sheridan, J.-C. Lin, and D. Rockwell. Flow past a cylinder close to a free surface. *Journal of Fluid Mechanics*, 330(2005):1–30, 1997. ISSN 00221120.

D. Sumner, E. Sprigings, J. Bugg, and J. Heseltine. Fluid forces on

BIBLIOGRAPHY

kayak paddle blades of different design. *Sports Engineering*, 6(1): 11–19, 2003.

R. Theunissen and R. Worboys. Near-wake observations behind azimuthally perforated disks with varying hole layout and porosity in smooth airstreams at high reynolds numbers. *Journal of Fluids Engineering*, 2018.

X. Tian, M. C. Ong, J. Yang, D. Myrhaug, and G. Chen. Three-dimensional effects of the flow normal to a flat plate at a high reynolds number. In *Proceedings of the ASME 2012 31st International Conference on Ocean, Offshore and Arctic Engineering, ASME, Rio de Janeiro, Brazil. 2012.* ASME, 2012.

S. Timoshenko. *History of strength of materials: with a brief account of the history of theory of elasticity and theory of structures*. Courier Corporation, 1983.

E. Tuck. Matching problems involving flow through small holes. *Advances in applied mechanics*, 15:89–158, 1975.

S. Vogel. Drag and flexibility and in sessile and organisms. *American Zoologist*, 24(1):37–44, 1984.

S. Vogel. Drag and reconfiguration of broad leaves in high winds. *Journal of Experimental Botany*, 40(8):941–948, 1989. doi: 10.1093/jxb/40.8.941.

H. von Helmholtz. Über discontinuirliche flüssigkeits-bewegungen. *Akademie der Wissenschaften zu Berlin*, 1868.

BIBLIOGRAPHY

C. E. Willert and M. Gharib. Digital particle image velocimetry. *Experiments in fluids*, 10(4):181–193, 1991.

H. Winter. Flow phenomena on plates and airfoils of short span. *NACA Technical Report 798*, 1936.

J. Xiong, A. Johnson, F. Liu, and D. Papamoschou. Body force model for the aerodynamics of inclined perforated surfaces. *AIAA Journal*, 50(11):2525–2535, nov 2012. doi: 10.2514/1.j051699.

X. Yu and A. Chwang. Water waves above submerged porous plate. *Journal of Engineering Mechanics*, 120(6):1270–1282, 1994.

UNIVERSITAT ROVIRA I VIRGILI
HYDRODYNAMICS OF FLAT PLATES IN CROSS-FLOW NEAR THE FREE SURFACE
Sukruth Satheesh